A Review of Bismuth-Rich Binary Oxides in the Systems Bi₂O₃–Nb₂O₅, Bi₂O₃–Ta₂O₅, Bi₂O₃–MoO₃, and Bi₂O₃–WO₃

Christopher D. Ling,[1] Ray L. Withers, Siegbert Schmid, and John G. Thompson

Research School of Chemistry, Australian National University, Canberra, Australian Capital Territory 0200, Australia

Bismuth-rich phases in the Bi₂O₃–Nb₂O₅, Bi₂O₃–Ta₂O₅, Bi₂O₃–MoO₃ and Bi₂O₃–WO₃ systems have been investigated using synchrotron X-ray diffraction (XRD) and electron diffraction (ED) to resolve outstanding problems concerning phase relationships, unit cells, and symmetry. A temperature-composition phase diagram for the Bi₂O₃–Nb₂O₅ system is presented. Single-phase powder specimens have been prepared for most phases. A modulated structure approach has been applied to the characterization of phases, and space groups or superspace groups assigned. The most appropriate description (commensurate modulation, incommensurate modulation or superstructure) for the structure of each of the phases is discussed. © 1998 Academic Press

INTRODUCTION

The high-temperature form of bismuth oxide, δ-Bi₂O₃, is recognized as one of the best solid-state oxygen ion conductors (1, 2). Although the pure phase cannot be quenched to room temperature, it is known that certain transition metal oxides, when added to Bi₂O₃ as the minor component, form binary oxides which often preserve a structure related to δ-Bi₂O₃ and retain its anionic conduction properties (3, 4). Such binary bismuth oxide phases are the focus of this study.

The structure of δ-Bi₂O₃ itself is not unambiguous. To a first approximation, it has a face-centred cubic (fcc) structure akin to fluorite (CaF₂) with an average oxygen occupancy of 75% (5) (Fig. 1). The oxygen vacancies in this model are supposed to account for its ionic conduction properties. More sophisticated oxygen vacancy-ordering models have been proposed and tested by the refinement of neutron powder diffraction data (6), but a definitive, fully ordered structure has yet to be established.

The Bi₂O₃-rich ends of binary oxide phase diagrams involving a range of transition metal oxides have been investigated on several levels. Studies using X-ray powder

diffraction (XRD) as the principal means of phase identification have been carried out in many systems. This approach has generally identified sillenite-related phases (7) at very low transition metal oxide concentration (below $\sim$ 5 mol%), succeeded by a series of solid solution fields of pseudo-fcc, fluorite-related phases (up to $\sim$ 30 mol%). Higher concentrations have led to non-fluorite-related structures such as the hexagonal close-packed (hcp) BiTaO₄ (8) and BiNbO₄ (9), and the (perovskite related) Aurivillius phases Bi₂WO₆ and γ-Bi₂MoO₆ (10). Despite similarities in behavior between different transition metal oxides, sufficient differences are observed to indicate that more complex mechanisms are involved than simple, non-stoichiometric substitution of metal atoms.

These subtleties were more clearly elucidated by a series of transmission electron microscope (TEM) studies in the Bi₂O₃–MoO₃ (11), Bi₂O₃–WO₃ (12), Bi₂O₃–Nb₂O₅ (13–18), and Bi₂O₃–Ta₂O₅ (17, 19) systems. In the TEM approach, the ability of electron diffraction (ED) to detect weak features of reciprocal space often missed by conventional powder diffraction methods is used to identify the modulations by which the average fluorite substructure is distorted, and to index reciprocal space in terms of fluorite superstructures. A greater number of discrete phases were thereby identified as possessing characteristic superstructures than had previously been identified by XRD. Furthermore, image contrast between metal atom sites in high resolution TEM (HRTEM) images was used to propose models for the superstructures in real space. As oxygen atoms were unresolved by HRTEM, the oxygen atom vacancies were modeled such that the substituting metal atoms (Nb, Ta, Mo, W) were octahedrally coordinated as in pyrochlore (20). Oxygen atoms coordinated only by Bi³⁺ were considered to remain in average fluorite positions.

The final class of experiment carried out in these systems has been single-crystal X-ray diffraction. To date, there have been very few actual single-crystal structure refinements. The average structure of Bi₃NbO₇ has been refined as being of fluorite-type (21); precession photography has been used to inform a cation ordering model for Bi₁₄W₂O₂₇ (22); and

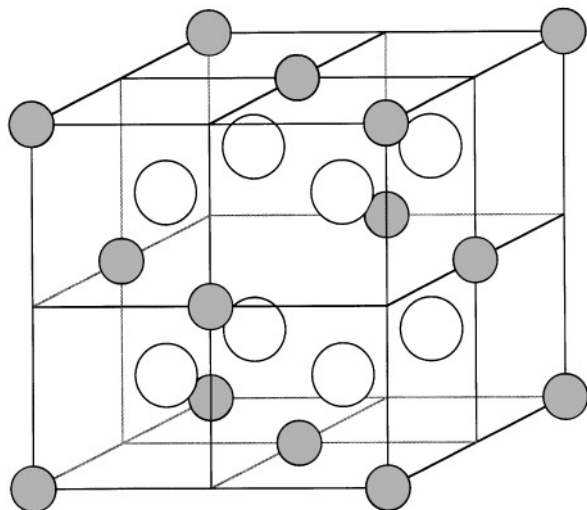---

[1]To whom correspondence is to be addressed.

FIG. 1. The 'average' structure of δ-Bi_2O_3; $Fm3m$, $a = 5.6595(4)$ Å (5). Oxygen sites (white) have 75% occupancy.

a single-crystal structure refinement has been published for $Bi_{26}Mo_{10}O_{69}$ (23).

The most-studied of these systems is $Bi_2O_3–Nb_2O_5$. The volume of work published does not, however, appear to have resulted in consensus; it has in fact highlighted some ambiguities and uncertainties, as a critical review of the literature shows. Published phase diagrams (24, 25) describe two solid-solution phases (approximately 0–20 and 20–23 mol% Nb_2O_5) and one line phase (37.5 mol% Nb_2O_5) between Bi_2O_3 and $BiNbO_4$. Subsequent ED studies (13–18) showed that the solid solutions described oversimplified the system and suggested the existence of at least four distinct structure types in this composition range. Type I was reported to exist between $Bi_{19}NbO_{31}$ and Bi_9NbO_{16} (13), but to predominate at $Bi_{15}NbO_{25}$. Type II was reported to exist between Bi_9NbO_{16} and Bi_3NbO_7 (13), $Bi_{24}Nb_2O_{41}$ and $Bi_8Nb_2O_{17}$ (14), or $Bi_{19}NbO_{31}$ and $Bi_{23}Nb_7O_{52}$ (15). An independent ED study (30) reported a composition range 11.2–26.6 mol% Nb_2O_5. Type III was reported to exist around 30 mol% Nb_2O_5 (with a disordered variant around 32 mol% Nb_2O_5), although energy dispersive X-ray analytical (EDXA) TEM work by the same authors suggested a composition closer to 25 mol% Nb_2O_5 (i.e., Bi_3NbO_7) (14). A single-crystal X-ray study (21) found a cubic phase (presumably type II) at the latter composition. Type IV, in accordance with the earlier XRD work, was found to occur at 5:3 (i.e., $Bi_5Nb_3O_{15}$) (17, 18).

In general, inconsistencies within the published work on the Bi_2O_3-rich end of the $Bi_2O_3–Nb_2O_5$ system are linked to inconsistencies between phase characterization on the bulk (starting materials, XRD) and microscopic (ED, EDXA) scales. Phases characterized by TEM need not originate from a homogeneous sample, and although their

compositions may be determined *in situ* by EDXA, doubts will persist as to their exact composition in bulk specimens. A pivotal aspect of the present study is therefore the requirement that results obtained by XRD (which provide structural and phase information on bulk specimens) are completely consistent with ED results (which provide structural and phase information from individual microcrystals within a specimen).

Given that most known phases at the Bi_2O_3-rich ends of the $Bi_2O_3–Nb_2O_5$, $Bi_2O_3–Ta_2O_5$, $Bi_2O_3–WO_3$ and $Bi_2O_3–MoO_3$ systems were initially characterized by TEM alone, the present work aims to review critically the results of previous studies on these systems, drawing together the information obtained using disparate techniques. There follows a reinvestigation of these systems involving synthesis, characterization using a combination of XRD and ED, and redescription of the various phases using a modulated structure approach. It is felt that the modulated structure approach allows more concise descriptions of some of the very large line-phase superstructures reported and provides insight into how the solid-solution structures accommodate the range of compositions in each case.

EXPERIMENTAL

Synthesis

Preliminary synthetic experiments carried out in the $Bi_2O_3–Nb_2O_5$ system using platinum crucibles as reaction vessels yielded inconsistent results. Single-phase bulk samples were elusive despite regrinding and annealing of reagents, and the unit cell dimensions of solid-solution phases were not reproducible. Quantitative EDXA analyses (using $BiNbO_4$ as a standard) of samples indicated significantly higher Nb_2O_5 content than expected based on the starting ratio of reagents, *e.g.*, starting materials with 14.3 mol% Nb_2O_5 heated to 1323 K for 3 days formed material analyzing at 16.7 mol% Nb_2O_5, and starting materials at 16.7 mol% Nb_2O_5 heated to 1173 K for 2 days formed products at 23.0 mol% Nb_2O_5. This indicated that the open system in which the reaction was taking place was allowing the uncontrolled loss of Bi_2O_3 through volatilization. The use of open reaction systems in earlier studies may explain some of the confusion concerning compositions of bulk specimens, *e.g.*, the type III phase reportedly synthesized at 30 mol% Nb_2O_5 but determined by EDXA to be 25 mol% Nb_2O_5 (14).

In order to achieve homogeneous, single-phase material, it is therefore necessary to limit the loss of starting materials (in particular Bi_2O_3) through volatilization. A simple and effective way of achieving this was to seal the reactants in platinum tubing (silica vessels being impractical due to the possibile formation of sillenite, $Bi_{12}SiO_{20}$). Although this limited the quantity of material reacted at any one time to

hundreds of milligrams, we could easily produce sufficient material for analysis. In addition, to ensure complete mixing of components without opening the sealed vessels for regrinding, samples were subjected to an initial annealing at 1103 K (just above the melting point of Bi_2O_3, 1098 K) in an open platinum vessel before being reground and sealed in platinum tubing.

In studies of the systems Bi_2O_3–Nb_2O_5, Bi_2O_3–Ta_2O_5, Bi_2O_3–WO_3, and Bi_2O_3–MoO_3, homogeneous samples of discrete line-phases and representatives of solid-solution phases reported in the literature were synthesized in quantities sufficient for XRD analysis. The results of previous XRD and ED/EDXA studies were used to suggest ratios of starting materials for syntheses. A summary of key syntheses is presented in Table 1. The results of syntheses excluded from Table 1 were consistent with those included, but redundant in terms of the conclusions drawn (*e.g.*, additional syntheses in two-phase regions).

Characterization

Identification of phases during synthetic work was based on XRD films collected using $CuK\alpha$ radiation ($\lambda = 1.54059$ Å) and a Guinier-Hägg camera. This method allowed collection of patterns from very small amounts of reaction products (< 1 mg), easy comparison of patterns by overlaying films, and visual identification of extremely weak modulation reflections. The necessity to measure line spacings manually and estimate intensities, however, made it a less attractive method for indexing the complex patterns which arise from large supercells.

Indexing of patterns and refinement of unit cells was for the most part carried out using synchrotron XRD data, collected at Beam Line 20B at the Photon Factory in Tsukuba, Japan. Each pattern was collected across three image plates at a wavelength of 1.4986 Å, from $2\theta \approx 5$ to $125°$. Si (NBS $\#$ 640) was used as an internal standard. Unit cell refinement and indexing was carried out with the Rietveld refinement program GSAS (26), fitting a model in which metal atoms of the substructure, fluorite-type δ-Bi_2O_3, were placed into the superstructure cell. As the strongest lines in most patterns correspond to the substructure dominated by metal atom scattering, this approach provided confirmation that the fluorite-type subcell had been identified correctly, and therefore that the indexing of weaker reflections to the often very large supercell was correct. Misindexing may otherwise easily happen when a large unit cell is used to index XRD reflections.

ED analyses were carried out using a JEOL 100CX TEM. EDXA analyses were carried out in a JEOL 6400 scanning electron microscope (SEM) equipped with a Link ATW detector at 15 kV and 1 nA, with data processed using the Link ISIS system. ZAF corrections were made using the SEM-QUANT software package.

Differential thermal analysis (DTA) experiments were performed in a Shimadzu DTA-50 instrument using a 20 mg sample in an alumina crucible with a platinum lid. A 20 mg sample of alumina was used in the second crucible. Dry argon was used to purge the system of oxygen for 20 min. prior to heating and flowed through the furnace chamber at 50 ml/min. throughout the heating cycle. The sample was heated to $100°C$ above the liquidus at $20°C$/min. and allowed to cool at the same rate.

RESULTS AND DISCUSSION

Phase Relationships

Bi_2O_3–Nb_2O_5. A partial temperature-composition phase diagram of the system was prepared from our results in the system Bi_2O_3–Nb_2O_5 (Fig. 2). Data for the temperature axis were obtained from DTA. This phase diagram deviates from the findings of the previous ED studies significantly. At the Bi_2O_3-rich end, type I was not observed; rather, a sillenite-related phase of composition $Bi_{12}Nb_{0.29}O_{18.7+x}$ (27) was found to be responsible for ED patterns qualitatively identical to those reported for type I (body-centered cubic). It became clear that this Bi_2O_3-rich phase was not δ-Bi_2O_3-related when the unit cell dimension was refined from XRD data, as $a = 10.048(1)$ Å, too small for a $2\mathbf{a}_f$, $2\mathbf{b}_f$, $2\mathbf{c}_f$ supercell of fluorite-type δ-Bi_2O_3 ($a = 5.6595(4)$ Å), which had previously been suggested for type I (13).

The Bi_2O_3-rich end member of the type II solid-solution was found to be $Bi_{15}NbO_{25}$. A plot of the underlying fluorite subcell dimension of the type II phase as a function of composition obeyed Vegard's law (Fig. 3) from $Bi_{15}NbO_{25}$ up to a narrow two-phase region with type III, consistent with type II being a solid solution. Quantitative EDXA analyses of specimens within the type II + type III two-phase region gave end-member compositions of 23.4(4) and 25.5(2) mol% Nb_2O_5 respectively, using $BiNbO_4$ as a standard.

Syntheses spanning the composition 25 mol% Nb_2O_5 confirmed that type III is a line phase of composition Bi_3NbO_7; previous syntheses with contradictory results (14) presumably suffered from loss of Bi_2O_3 and therefore arrived at more Nb_2O_5-rich compositions. Type IV was also found to be a line phase ($Bi_5Nb_3O_{15}$) with an upper temperature limit of stability; above the transition temperature between the high- and low-temperature modifications of $BiNbO_4$ ($1020°C$) (9), type IV was found to unmix into type III and $BiNbO_4$(H) (28).

Bi_2O_3–Ta_2O_5. We found four line phases between Bi_2O_3 and $BiTaO_4$, at $Bi_{15}TaO_{25}$, $Bi_7Ta_3O_{18}$, $Bi_4Ta_2O_{11}$, and $Bi_{31}Ta_{17}O_{89}$, and a solid-solution between Bi_9TaO_{16} and Bi_3TaO_7. The only published phase diagram in this

TABLE 1
Selective Summary of Syntheses Carried out in this Study. Parenthesized Phases Have a Trace Presence.
'S' Indicates Sillenite-related Phases, '38:7' and '26:10' Represent $Bi_{38}Mo_7O_{78}$ (11) and $Bi_{26}Mo_{10}O_{69}$ (23) Respectively

| Binary system (+ Bi_2O_3)	Minor oxide (Mol %)	Final annealing Temp (K)	Final annealing Time (h)	Phases identified by XRD	Comments
Ta_2O_5	6.25	1098	72	I	type I nominal composition (19)
	19.53	1173	360	II	type II nominal ss composition (19)
	19.53	1273	72	(I), II	type II unstable at 1000°C
	30.00	1173	192	II*	type II* nominal composition (19)
	30.00	1273	72	(II), II*	type II* unstable at 1000°C
	33.33	1173	192	III	type III nominal composition (19)
	33.33	1273	72	(II*), III	type III unstable at 1000°C
	35.42	1273	168	IV	type IV nominal composition (17)
	37.50	1173	144	III, L–BiTaO$_4$	type IV not formed at 900°C
	37.50	1273	144	IV, (H–BiTaO$_4$)	
W_2O_6	6.67	1103	192	Ia	type Ia nominal composition (12)
	12.50	1173	192	Ib	type Ib nominal composition (12)
	14.81	1073	48	Ib	type Ib ss: II nominal composition (12)
	14.81	1173	168	Ib	type Ib ss: II nominal composition (12)
	15.38	1173	192	Ib	type Ib ss
	16.00	1173	168	Ib	type Ib ss
	16.67	1098	120	Ib, II	
	18.19	1173	192	II, (Bi$_2$WO$_6$)	
Mo_2O_6	6.67	1073	168	Ia	type Ia nominal composition (30)
	12.50	1173	96	38:7	38:7 highly disordered ss
	14.29	1173	96	38:7	38:7 partially disordered ss
	15.55	1113	168	38:7	38:7 nominal composition (11)
	16.66	1173	96	38:7, (26:10)	
	25.00	1113	168	(38:7), 26:10	
	27.78	1173	168	26:10	26:10 nominal composition (23)
Nb_2O_5	1.00	1073	48	δ-Bi$_2$O$_3$, S	
	1.96	1173	120	S, (II)	
	4.76	1098	144	(S), II	
	4.76	1173	120	(S), II	
	6.25	1173	120	II	type I nominal composition (13): II ss
	6.25	1273	120	(S), II	type II ss end-member unstable at 1000°C
	7.69	1093	24	II	type II ss
	9.09	1093	24	II	type II ss
	10.00	1093	96	II	type II ss (15)
	11.11	1093	24	II	type II ss
	15.00	1093	96	II	type II ss (15)
	16.67	1173	48	II	type II ss
	20.00	1093	96	II	type II ss (15)
	22.22	1173	48	II	type II ss
	23.53	1173	48	II, III	
	25.00	1173	96	III	type III nominal composition (14)
	28.57	1173	96	III, (IV)	
	36.36	1173	24	(III), IV	
	37.50	1173	240	IV	type IV nominal composition (17)
	37.50	1273	96	IV	type IV nominal composition (17)
	37.50	1343	120	III, H–BiNbO$_4$	type IV unstable at 1050°C
	40.00	1173	24	IV, (L–BiNbO$_4$)	
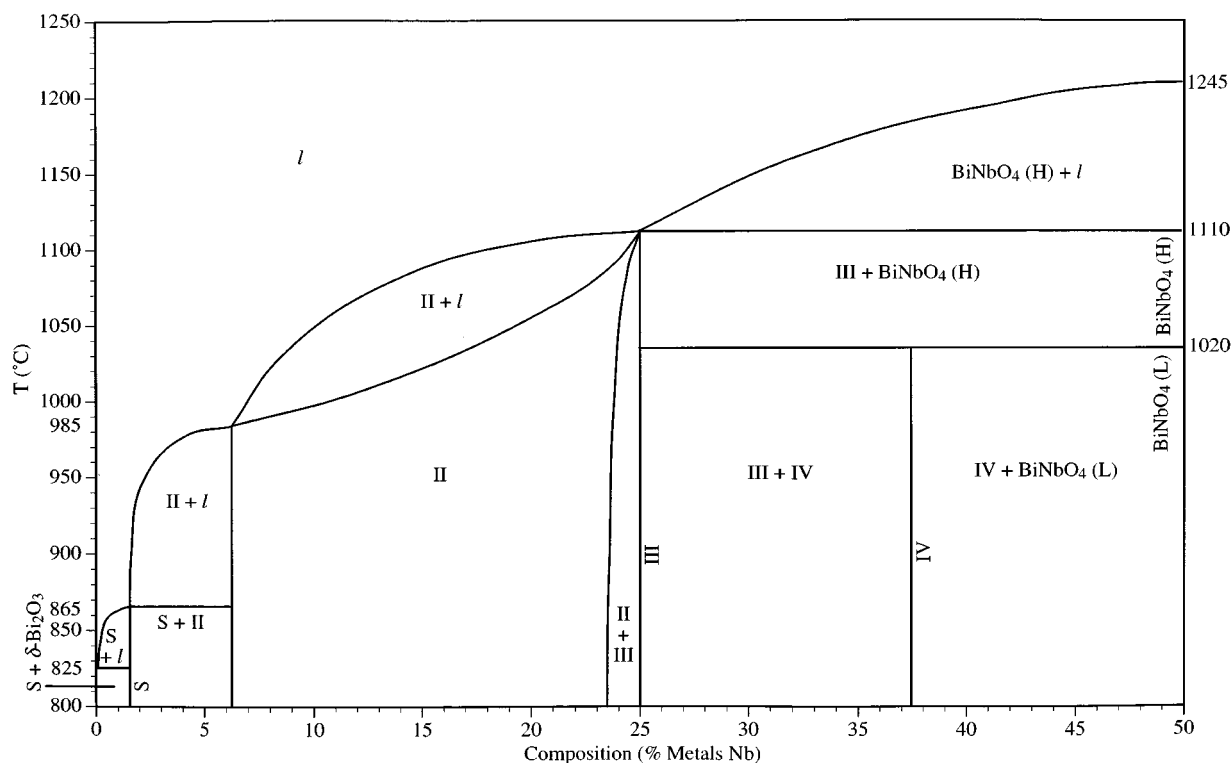
FIG. 2. Partial phase diagram of the Bi_2O_3–Nb_2O_5 system. 'S' is a sillenite-type phase, 'L' and 'H' are the low- and high- temperature forms of $BiNbO_4$ respectively.

system (25) focuses on the extremely Bi_2O_3-rich region, dominated by a sillenite-related solid-solution phase, and does not discuss these phases.

Previous ED studies (17, 19) report these phases as δ-Bi_2O_3-related, labeling them types I ($Bi_{15}TaO_{25}$), II (Bi_9TaO_{16} to Bi_3TaO_7), II* ($Bi_7Ta_3O_{18}$), III ($Bi_4Ta_2O_{11}$), and IV ($Bi_{31}Ta_{17}O_{89}$). Type III was understood to be metastable (17), but our synthetic regime allowed preparation of single-phase powder specimens of this phase along with types I, II, II*, and IV.

Bi_2O_3–WO_3. Three phases were observed between Bi_2O_3 and Bi_2WO_6 in addition to a β-Bi_2O_3-related solid-solution at compositions close to Bi_2O_3: a line phase at $Bi_{14}WO_{24}$; a solid-solution phase between $Bi_{42}W_8O_{87}$ and $Bi_{30}W_4O_{57}$; and a line phase at approximately $Bi_{34}W_8O_{75}$. The latter was not obtained as a single-phase, but was observed by XRD in a two-phase mixture with trace amounts of the solid-solution phase for the synthesis at 16.67 mol% W_2O_6 and trace amounts of Bi_2WO_6 at 18.19 mol% W_2O_6.

The most recent published phase diagram of this system (29) reports line phases at $Bi_{12}WO_{21}$ and Bi_4WO_9, most likely corresponding to the line phases observed (at similar compositions) in this study. A solid-solution is reported centered on Bi_6WO_{12}, with a subsequent investigation (22)

placing its range between 11.90 and 15.15 mol% W_2O_6 in reasonable agreement with our results. Recent ED work (12) describes types Ia ($Bi_{14}WO_{24}$), Ib ($Bi_{24}W_2O_{33}$–Bi_6WO_{12}), and II* ($Bi_{46}W_8O_{93}$). Type Ia clearly corresponds to the phase observed in this study at the same composition, and type Ib to the solid-solution phase. The higher Bi_2O_3 content previously reported for the solid-solution range may again be due to the use of open vessels and subsequent Bi_2O_3 loss. The reported composition of type II* is also too Bi_2O_3-rich to be compatible with our observations (presumably for the same reason), falling within the range observed for type Ib. The line phase observed in this study at approximately 17.5 mol% W_2O_6 appears to correspond to type II* according to our ED results discussed below, but has different composition.

In light of the apparent success of this study in controlling composition, it is somewhat surprising to note that the phases described in the phase diagram discussed above are Bi_2O_3-poor compared to our observations. The reason for this discrepancy is unclear.

Bi_2O_3–MoO_3. Three line phases were observed between Bi_2O_3 and Bi_2MoO_6, at $Bi_{14}MoO_{24}$, $Bi_{38}Mo_7O_{78}$, and $Bi_{26}Mo_{10}O_{69}$. Between 14.29 and 15.56 mol% Mo_2O_6 (*i.e.*, $Bi_{38}Mo_7O_{78}$), reaction kinetics were found to be sufficiently
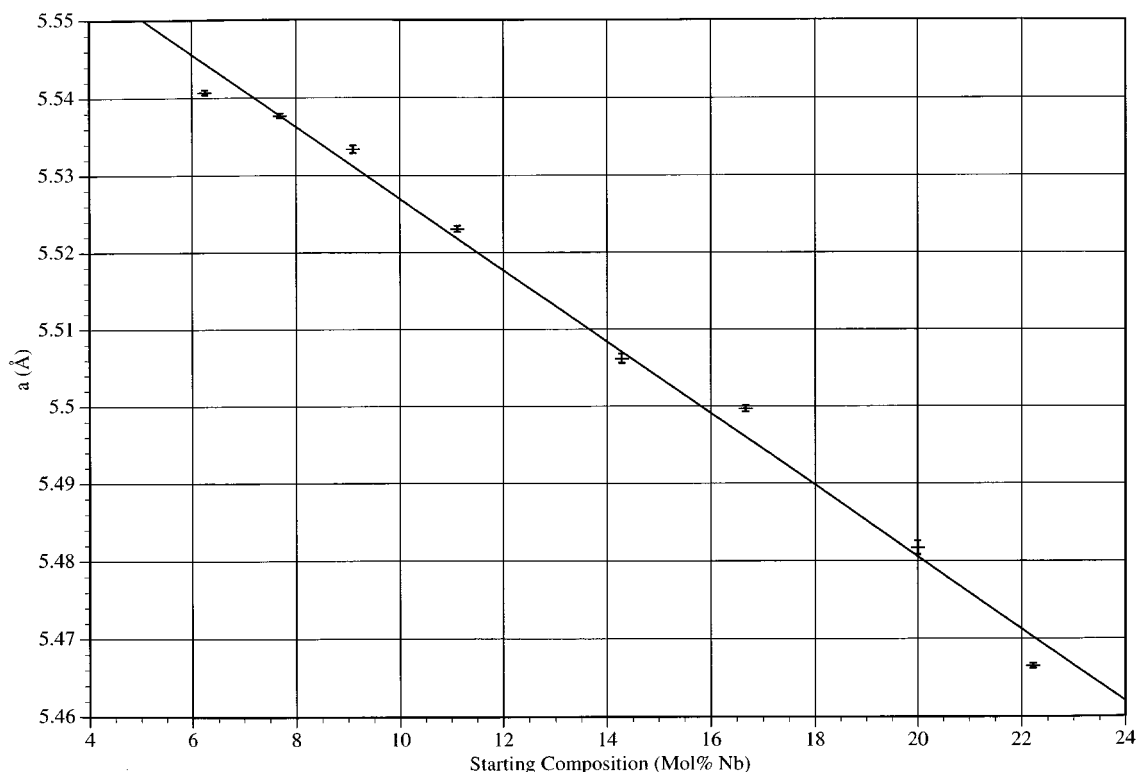
FIG. 3. Vegard's law behavior of the type II solid-solution phase in the Bi$_2$O$_3$–Nb$_2$O$_5$ system.

slow that well crystallized material could not be obtained; however, below 14.29 mol% Mo$_2$O$_6$, a clear two-phase region with Bi$_{14}$MoO$_{24}$ was observed as expected. The presence of three phases is in agreement with the most recent XRD-based phase diagram of this system (30), which reported line phases Bi$_{14}$MoO$_{24}$, Bi$_6$MoO$_{12}$, and Bi$_6$Mo$_2$O$_{15}$. The first of these has been neither indexed nor investigated by ED, but its composition and XRD pattern suggest an analog to the type Ia phase in the Bi$_2$O$_3$–WO$_3$ system. A single-crystal X-ray structure of Bi$_{26}$Mo$_{10}$O$_{69}$ has been published (23). Bi$_{38}$Mo$_7$O$_{78}$ has been reported as a line phase in an ED study (11).

Electron Diffraction

Bi$_2$O$_3$–Nb$_2$O$_5$. Integer indexation of the reciprocal lattice of the type II solid-solution phase (**FIG. 4**) requires six basis vectors given by $M^* = \mathbf{a}_f^*, \mathbf{b}_f^*, \mathbf{c}_f^*, \varepsilon\mathbf{a}_f^*, \varepsilon\mathbf{b}_f^*$, and $\varepsilon\mathbf{c}_f^*$, respectively, where the subscript f refers to the fluorite type substructure and $\varepsilon \approx 0.37$ (31, 32). Any Bragg reflection **H** can thus be written in the form $\mathbf{H} = h\mathbf{a}_f^* + k\mathbf{b}_f^* + l\mathbf{c}_f^* + m\varepsilon\mathbf{a}_f^* + n\varepsilon\mathbf{b}_f^* + p\varepsilon\mathbf{c}_f^* = [h\,k\,l\,m\,n\,p]^*$ with h, k, l, m, n, and p all integers. The structure at any particular composition within the solid solution is thus a three-dimensional incommensurately modulated structure characterized by a six-

dimensional superspace group symmetry (32, 33). There are very few other known examples of three-dimensional incommensurately modulated structures (34, 35).

The observed characteristic extinction conditions $F([h\,k\,l\,m\,n\,p]^*) = 0$ unless $h + k, k + l, h + l, m + n, n + p$, and $m + p$ are all even and $F(\langle h\,k\,0\,m\,n\,0\rangle^*) = 0$ unless $m + n = 4J, J$ an integer (Fig. 4d), in conjunction with the overall $m3m$ Laue symmetry of reciprocal space, imply a six-dimensional superspace group symmetry $P:Fm\bar{3}m: Fd\bar{3}m$, (in the notation of Yamamoto (34)). The first F in this superspace group symbol implies that the allowed Bragg reflections, $\mathbf{G}_f = h\mathbf{a}_f^* + k\mathbf{b}_f^* + l\mathbf{c}_f^*$, of the underlying fluorite-type substructure obey fcc extinction rules. The second F implies that the allowed satellite reflections decorating these allowed substructure reflections also obey fcc extinction rules (Figs. 4c, 4d). The first allowed, or 'primary', modulation wave-vectors are thus of the form $\mathbf{q}_i = \varepsilon\langle 1\,1\,1\rangle^*$. Note that the most intense satellite reflections (Fig. 4) are invariably first order harmonic (*i.e.*, of the form $\mathbf{G}_f \pm \mathbf{q}_i$) and decay rapidly with increasing harmonic order.

The d-hyperglide superspace symmetry operations of the form $\{x_1, x_2, -x_3, x_4 + 1/4, x_5 + 1/4, -x_6\}$ (responsible for the $F(\langle h\,k\,0\,m\,n\,0\rangle^*) = 0$ unless $m + n = 4J$ extinction conditions) provide an important constraint on the form of
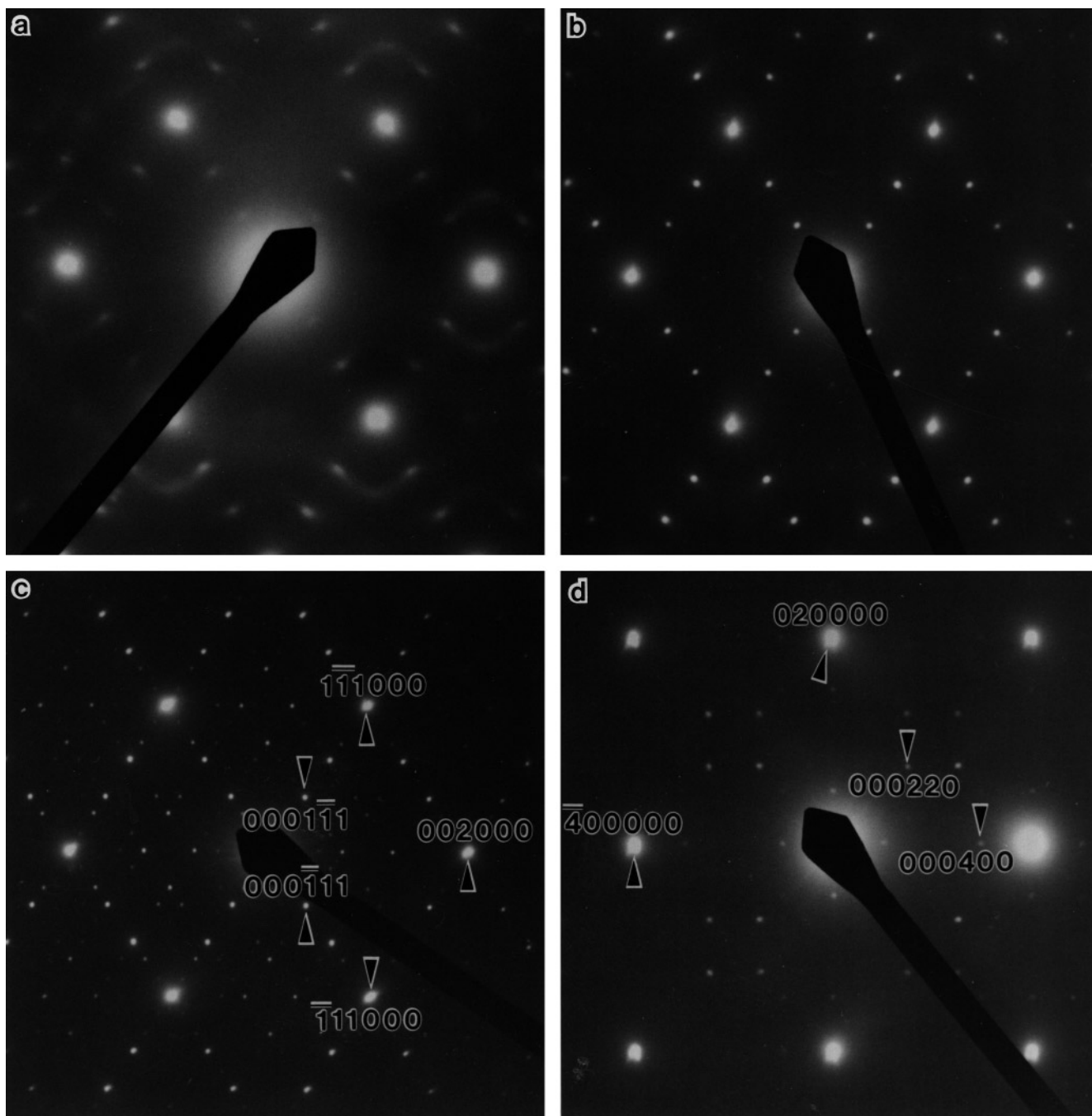
FIG. 4. $\langle 1 1 0 \rangle_f$ zone axis DPs of the type II phase in the Bi_2O_3–Nb_2O_5 system at compositions $Bi_{15}NbO_{25}$ (a), $Bi_{17}Nb_3O_{33}$ (b), and $Bi_8Nb_2O_{17}$ (c). (d) $\langle 0 0 1 \rangle_f$ zone axis of $Bi_{17}Nb_3O_{33}$ showing extinctions due to a d-glide in the modulation.

the compositional and displacive atomic modulation functions (AMFs), which describe the deviation of the actual crystal structure at any particular composition from its underlying fluorite-type substructure (32, 34, 35). For an example of how such a hyperglide symmetry operation constrains the form of the corresponding AMFs, see Withers *et al.* (35).

Careful measurement of DPs such as those of Fig. 4 suggests that the magnitude of ε increases smoothly and monotonically with composition across the whole composition range, from 6.25 to 23.4 mol% Nb_2O_5. Miida and Tanaka (36) reported that ε increased smoothly and monotonically for $0.13 \leq x \leq 0.24$, but was nearly constant outside this

range. The intensity of the primary $\mathbf{G}_f \pm \mathbf{q}_i$ satellite reflections, as well as the anharmonic character of the modulated structure (*i.e.*, the visibility of higher order harmonic satellite reflections), also appear to increase smoothly and monotonically across the whole composition range (Figs. 4a–4c). Note also the disorder evident in the diffuse streaking accompanying the primary $\mathbf{G}_f \pm \mathbf{q}_i$ satellite reflections at low Nb$_2$O$_5$ content (Fig. 4a).

Previous authors (13, 15) have used image simulation techniques at high Nb$_2$O$_5$ content and DP simulation at low Nb$_2$O$_5$ content to propose plausible commensurate superstructure models based on idealized cubic $8\mathbf{a}_f$, $8\mathbf{b}_f$, $8\mathbf{c}_f$ (Bi$_8$Nb$_2$O$_{17}$) or $11\mathbf{a}_f$, $11\mathbf{b}_f$, $11\mathbf{c}_f$ (Bi$_9$NbO$_{16}$, Bi$_{17}$Nb$_3$O$_{33}$) supercells of fluorite-type δ-Bi$_2$O$_3$. It is important to realize, however, that compositions at which ε apparently coincides with rational fractions such as 3/8 or 4/11 do not imply that ε has 'locked in' to a commensurate value. The real test of commensurability is rather whether all possible higher order harmonic satellite reflections can be observed, *i.e.*, whether there is 'overlap' or interaction between modulated intensity arising from independent subcell reflections (32). In the current case, this would necessitate observation of at least fourth-order harmonics of $\mathbf{q}_i$ (when $\varepsilon = 3/8$). In practice, only a maximum of third order satellite reflections is ever observed in DPs, even fewer in XRD data (Fig. 4c). These structures are effectively incommensurate regardless of the apparent value of ε.

While the type II phase is clearly an incommensurate, 'infinitely adaptive' solid solution, it is interesting to note that the disordered fluorite-to-pyrochlore ($A_2B_2X_7$) transformation involving coupled A/B metal ion and oxygen vacancy ordering (37), on which structural models for this type II phase have been based (13, 15), can be described by the same three-dimensional modulation and six-dimensional superspace group but with ε genuinely 'locked in' at $\varepsilon = 1/2$.

$\langle 1\,1\,0 \rangle$, $\langle 1\,0\,0 \rangle$, and $[0\,0\,1]$ zone axis micro-diffraction patterns (MDPs) characteristic of the tetragonal type III line phase Bi$_3$NbO$_7$ are shown indexed with respect to an $\mathbf{a} = 3\mathbf{a}_f$, $\mathbf{b} = 3\mathbf{b}_f$, $\mathbf{c} = 7\mathbf{c}_f$ fluorite supercell in Figs. 5a, 5c, and 5d respectively. Similar, but unindexed, selected area DPs have been published previously (14). This $3 \times 3 \times 7$ cell is clearly F-centered with a most probable space group symmetry of $F4/mmm$. As pointed out by Zhou *et al.* (14), the standard setting for this space group is $I4/mmm$ with $\mathbf{a}' = \frac{3}{2}(\mathbf{a}_f - \mathbf{b}_f)$, $\mathbf{b}' = \frac{3}{2}(\mathbf{a}_f + \mathbf{b}_f)$, $\mathbf{c}' = 7\mathbf{c}_f$.

The non-standard setting for type III is used in order to emphasize the close relationship of type III to Nb$_2$O$_5$-rich type II, as shown by a comparison of the $\langle 1\,1\,0 \rangle$ zone axis MDP of type II at 20 mol% Nb$_2$O$_5$ (Fig. 5b) with the corresponding $[1\,1\,0]$ zone axis MDP of type III (Fig. 5a). The reciprocal lattices of both phases are characterized by a very similar hierarchical intensity distribution. The only obvious distinction is that the $\mathbf{q}_i \approx 0.38\langle 1\,1\,1 \rangle^* =$

$\langle 0.38\,0.38\,0.38 \rangle^*$ 'primary' modulation wave-vectors of type II have rotated slightly and 'locked in' to $\langle \frac{1}{3}\frac{1}{3}\frac{3}{7} \rangle^*$ positions in the case of the (tetragonal) type III (*cf.* Fig. 5a *vs* Fig. 5b). An orientationally variable primary modulation wave-vector has recently also been reported in the case of the sulfosalt mineral sartorite (38). It seems clear that a successful structure refinement of type III will necessarily provide great insight into the nature of type II.

The type IV (Bi$_5$Nb$_3$O$_{15}$) line phase was found to be a one-dimensional, incommensurately modulated structure characterized by an incommensurate primary modulation wave-vector $\mathbf{q} \approx 0.18\mathbf{a}^* + 0.04\mathbf{b}^* + \mathbf{c}^*$ and a very close to metrically tetragonal (no peak splitting is observed in XRD), body-centred cubic, average structure (Fig. 6, Table 2). The incommensurate nature of the primary modulation wave-vector along both the $\mathbf{a}^*$ and $\mathbf{b}^*$ directions of reciprocal space was quite reproducible from grain to grain for our synthetic conditions and necessarily lowers the average structure space group symmetry to at most monoclinic $I112/m$. The most probable superspace group symmetry is $I112/m(0.18, 0.04, 1)\bar{1}1$. This is a nonstandard superspace group setting; it is retained due to the demonstrated relationship (17, 18) to the Aurivillius family of phases, making a change of setting inappropriate.

Zhou *et al.* (17) reported two distinct type IV phases; an $a = 31.79$, $b = 5.45$, $c = 41.02$ Å orthorhombic structure (corresponding to a primary modulation wave-vector $\mathbf{q} = \frac{1}{6}\mathbf{a}^* + \mathbf{c}^*$) and a monoclinic type IV* variant. The DPs of Fig. 5 are most closely related to those reported for the former, except for the incommensurability of the primary modulation wave-vector along the $\mathbf{b}^*$ direction. Exactly what factor controls the apparent variability in the observed primary modulation wave-vector remains unclear.

Bi$_2$O$_3$–Ta$_2$O$_5$. ED work with the type I phase in this system identified the commensurate modulation reported (19), leading to a $2\mathbf{a}_f$, $2\mathbf{b}_f$, $2\mathbf{c}_f$ I-centered supercell of fluorite-type δ-Bi$_2$O$_3$. The space group could not be uniquely determined ($I23$, $I2_13$, $Im\bar{3}$, $I432$, $I\bar{4}3m$ or $Im\bar{3}m$). Type II was also found as reported, apparently isomorphous to the type II phase in the Bi$_2$O$_3$–Nb$_2$O$_5$ system described above and subject to the same argument for an incommensurately modulated structure description.

Indexation of DPs of the large unit cell, low symmetry, type II* phase (Fig. 7) was nontrivial and required close cross-correlation between XRD data (Fig. 13) and ED data to ensure self-consistency. A unique C-centered monoclinic cell (most probable space group symmetry $C2/m$, $a \approx 34.0$, $b \approx 7.61$, $c \approx 6.63$ Å, $\beta \approx 109.2°$, was found to be the only possible solution (Figs. 7, 13). These DPs could not be indexed to the previously reported (19) simple fluorite-type superstructure ($\mathbf{a} = 5\mathbf{a}_f - 5\mathbf{b}_f$, $\mathbf{b} = \mathbf{a}_f + \mathbf{b}_f$, $\mathbf{c} = -\mathbf{a}_f + \mathbf{b}_f + 2\mathbf{c}_f$: $\mathbf{a}^* = \frac{1}{10}[1\,\bar{1}\,1]_f^*$, $\mathbf{b}^* = \frac{1}{4}[2\,2\,0]_f^*$, $\mathbf{c}^* = \frac{1}{4}[0\,0\,2]_f^*$: $a = 38.5$, $b = 7.70$, $c = 13.64$ Å, $\beta = 124.33°$), or indeed to any
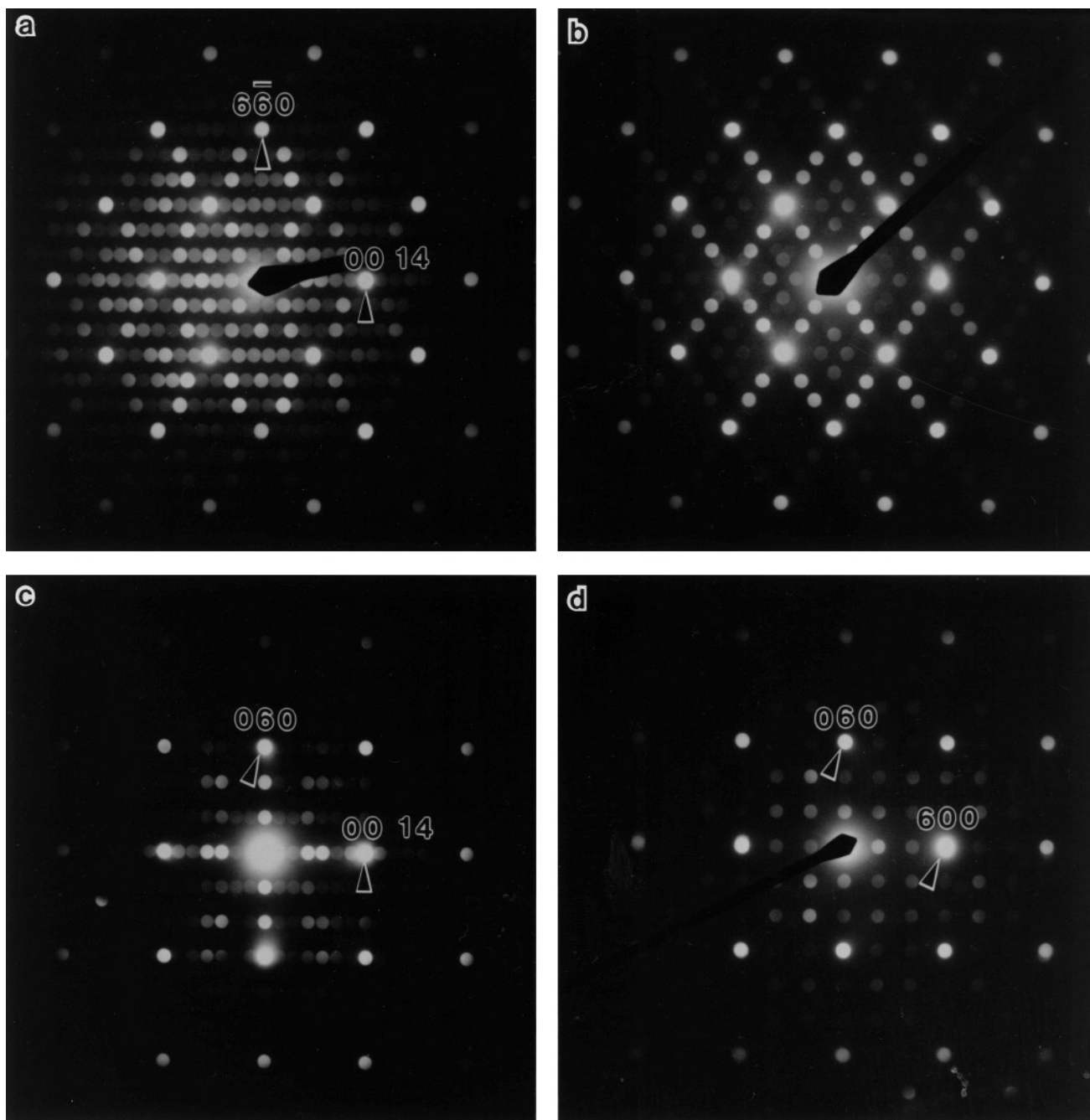
FIG. 5. (a) $\langle 1\,1\,0 \rangle_f$, $\langle 1\,0\,0 \rangle_f$, and $[0\,0\,1]_f$ zone axis DPs of the type III phase in the Bi_2O_3–Nb_2O_5 system. (b) Shows a $\langle 1\,1\,0 \rangle_f$ zone axis DP of the type II phase at the composition $Bi_8Nb_2O_{17}$.

other simple fluorite type superstructure, despite the observance of apparent fluorite-like zone axis DPs.

Consider, for example, Fig. 7b, which resembles a $\langle 1\,1\,0 \rangle_f$ zone axis DP and Fig. 7c, which resembles a $[\bar{1}\,1\,2]_f$ zone axis DP. The strong reflections labeled $[10,0,0]^*$ and $[0\,0\,2]^*$ in Fig. 7b appear to correspond to $\langle 1\,1\,1 \rangle_f^*$ average structure reflections (which should therefore be strong re-

flections, consistent with the XRD data in Fig. 13), while the strong reflection labeled $[0\ 4\ 0]^*$ in Fig. 7c appears to correspond to a $\langle 2\,2\,0 \rangle_f^*$ average structure reflection (also consistent with XRD data). The implied relationship between the reciprocal lattice of the apparent fluorite-type average structure and the actual reciprocal lattice is thus: $\mathbf{a}^* = \frac{1}{10}[1\,\bar{1}\,1]_f^*$, $\mathbf{b}^* = \frac{1}{4}[2\,2\,0]_f^*$, $\mathbf{c}^* = \frac{1}{2}[1\,\bar{1}\,\bar{1}]_f^*$. The
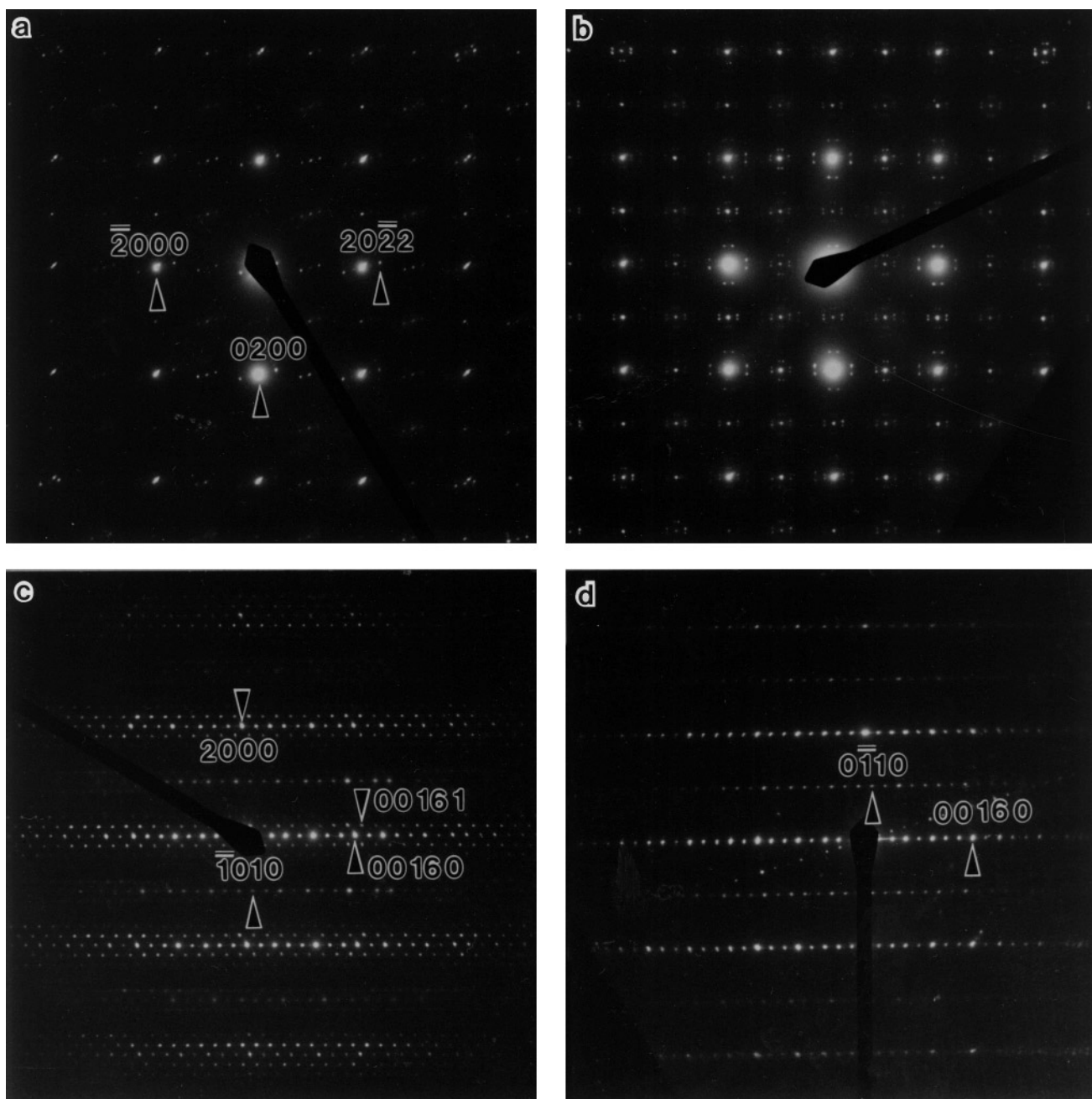
FIG. 6. (a) [0 0 1]$_f$, (c) [0 1 0]$_f$, and (d) [1 0 0]$_f$ zone axis DPs of the type IV phase in the Bi$_2$O$_3$–Nb$_2$O$_5$ system. (b) Shows a multiply twinned [0 0 1]$_f$ zone axis DP of the same phase.

problem with this apparent fluorite-type supercell is that the other strong $\langle 1\,1\,1 \rangle_f^*$ reflection expected in XRD data for a resultant monoclinic supercell, namely $[1\,1\,1]_f^* = [5\,2\,\bar{1}]^*$, is forbidden by the C-centering of the resultant supercell. The third strong $\langle 1\,1\,1 \rangle_f^*$ reflection observed in XRD and ED (Fig. 7d) data indexes as $[6\,2\,\bar{1}]^* = 1/20[22, 18, 22]_f^*$. Such problems were always encountered when the type II*

phase was assumed to possess an underlying, fluorite-type average structure.

Similar problems were encountered interpreting DPs of type III (Fig. 8). Indexation again required close cross-correlation between XRD (Fig. 14) and ED data to ensure self-consistency. A unique B-centered triclinic, but pseudo-monoclinic, cell (most probable space group symmetry $B1$

TABLE 2
Summary of Data Gathered in this Study, Referenced to Relevant Earlier Studies.

Minor oxide	Corresponding literature phase	Relationship to fluorite: Commensurate supercell or incommensurate modulation	Space group symmetry	Refined supercell (commensurate) or subcell (incommensurate) dimensions					
				a (Å)	b (Å)	c (Å)	α (°)	β (°)	γ (°)
Nb_2O_5	Bi_9NbO_{16}(15)	$\mathbf{q}_1 = \varepsilon\mathbf{a}_f^*,\ \mathbf{q}_2 = \varepsilon\mathbf{b}_f^*,\ \mathbf{q}_3 = \varepsilon\mathbf{c}_f^*:\ \varepsilon = 0.354$	$P:Fm\bar{3}m:$ $Fd\bar{3}m$	5.53057(4)	5.53057(4)	5.53057(4)	90	90	90
	$Bi_{17}Nb_3O_{33}$(15)	$\mathbf{q}_1 = \varepsilon\mathbf{a}_f^*,\ \mathbf{q}_2 = \varepsilon\mathbf{b}_f^*,\ \mathbf{q}_3 = \varepsilon\mathbf{c}_f^*:\ \varepsilon = 0.364$	$P:Fm\bar{3}m:$ $Fd\bar{3}m$	5.51044(3)	5.51044(3)	5.51044(3)	90	90	90
	$Bi_8Nb_2O_{17}$(15)	$\mathbf{q}_1 = \varepsilon\mathbf{a}_f^*,\ \mathbf{q}_2 = \varepsilon\mathbf{b}_f^*,\ \mathbf{q}_3 = \varepsilon\mathbf{c}_f^*:\ \varepsilon = 0.375$	$P:Fm\bar{3}m:$ $Fd\bar{3}m$	5.48632(3)	5.48632(3)	5.48632(3)	90	90	90
	Bi_3NbO_7 (14)	$\mathbf{a} = 3\mathbf{a}_f,\ \mathbf{b} = 3\mathbf{b}_f,\ \mathbf{c} = 7\mathbf{c}_f$	$F4/mmm$	16.31799(18)	16.31799(18)	38.5420(5)	90	90	90
	$Bi_5Nb_3O_{15}$(17)	ambiguous: $\mathbf{q} = \pm(0.18\ 0.04\ 1)^*$	$I112/m\mathbf{q}\bar{1}\,1$	5.4663(13)	5.4669(13)	41.9658(4)	90.06(2)	89.96(4)	90.014(12)
Ta_2O_5	$Bi_{15}TaO_{25}$(19)	$\mathbf{a} = 2\mathbf{a}_f,\ \mathbf{b} = 2\mathbf{b}_f,\ \mathbf{c} = 2\mathbf{c}_f$	$I{-}{-}{-}$	11.078(2)	11.078(2)	11.078(2)	90	90	90
	$Bi_{103}Ta_{25}O_{217}$(19)	$\mathbf{q}_1 = \varepsilon\mathbf{a}_f^*,\ \mathbf{q}_2 = \varepsilon\mathbf{b}_f^*,\ \mathbf{q}_3 = \varepsilon\mathbf{c}_f^*:\ \varepsilon = 0.375$	$P:Fm\bar{3}m:$ $Fd\bar{3}m$	5.47100(3)	5.47100(3)	5.47100(3)	90	90	90
	$Bi_7Ta_3O_{18}$(19)	ambiguous	$Cm,\ C2/m$	33.9870(9)	7.59960(19)	6.63082(17)	90	109.1485(12)	90
	$Bi_4Ta_2O_{11}$(19)	ambiguous	$B\bar{1},\ B\bar{1}$	7.6607(7)	6.6112(6)	19.7648(17)	89.791(3)	101.060(3)	90.020(3)
	$Bi_{31}Ta_{17}O_{89}$ (17)	ambiguous: $\mathbf{q} = \pm(0.04\ 0\ 0.75)^*$	$I12/m1\mathbf{q}\bar{1}\,1$	3.9033(5)	3.8561(4)	5.2027(8)	90	91.318(12)	90
WO_3	$Bi_{14}WO_{24}$(12)	$\mathbf{a} = \frac{3}{2}\mathbf{a}_f - \frac{1}{2}\mathbf{b}_f,\ \mathbf{b} = \frac{1}{2}\mathbf{a}_f + \frac{3}{2}\mathbf{b}_f,\ \mathbf{c} = 3\mathbf{c}_f$	$I{-}{-}{-}$	8.71355(8)	8.71355(8)	17.32527(18)	90	90	90
	$Bi_{14}W_2O_{27}$(12)	$\mathbf{a} = 2\mathbf{a}_f + \mathbf{b}_f,\ \mathbf{b} = -\mathbf{a}_f + 2\mathbf{b}_f,\ \mathbf{c} = 2\mathbf{c}_f$	$I4_1$	12.49577(11)	12.49577(11)	11.24641(10)	90	90	90
	$Bi_{46}W_8O_{93}$(12)	$\mathbf{a} = 3\mathbf{a}_f,\ \mathbf{b} = 3\mathbf{b}_f,\ \mathbf{c} = 3\mathbf{c}_f$	$F{-}{-}{-}$	16.68774(18)	16.68774(18)	16.6451(2)	90	90	90
MoO_3	$Bi_{14}MoO_{24}$ (30)	$\mathbf{a} = \frac{3}{2}\mathbf{a}_f - \frac{1}{2}\mathbf{b}_f,\ \mathbf{b} = \frac{1}{2}\mathbf{a}_f + \frac{3}{2}\mathbf{b}_f,\ \mathbf{c} = 3\mathbf{c}_f$	$I{-}{-}{-}$	8.7142(5)	8.7142(5)	17.3305(10)	90	90	90
	$Bi_{38}Mo_7O_{78}$ (11)	$\mathbf{a} = 3\mathbf{a}_f,\ \mathbf{b} = 5\mathbf{b}_f,\ \mathbf{c} = 3\mathbf{c}_f$	$Pccn$	16.8065(2)	28.6009(4)	16.8898(2)	90	90	90
	$Bi_{26}Mo_{10}O_{69}$ (23)	$\mathbf{a} = \frac{3}{2}\mathbf{a}_f + \frac{3}{2}\mathbf{c}_f,\ \mathbf{b} = \mathbf{b}_f,\ \mathbf{c} = -4\mathbf{a}_f + 2\mathbf{c}_f$	$P2/c$	11.74130(10)	5.80071(6)	24.7940(2)	90	102.8442(4)	90

or $B\bar{1}$), $a \approx 7.66$, $b \approx 6.61$, $c \approx 19.765$ Å, $\alpha \approx 89.8$, $\beta \approx 109.2$, $\gamma \approx 90.02°$, was found to be the only possible solution. Again, DPs could not be indexed to the previously reported (19) simple fluorite superstructure ($\mathbf{a} = 3\mathbf{a}_f - 3\mathbf{b}_f$, $\mathbf{b} = 2\mathbf{a}_f + 2\mathbf{b}_f$, $\mathbf{c} = -\mathbf{a}_f + \mathbf{b}_f + 2\mathbf{c}_f$; $\mathbf{a}^* = \frac{1}{6}[1\,\bar{1}\,1]_f^*$, $\mathbf{b}^* = \frac{1}{8}[2\,2\,0]_f^*$, $\mathbf{c}^* = \frac{1}{4}[0\,0\,2]_f^*$, $a = 24.14$, $b = 14.63$, $c = 13.47$ Å, $\beta = 126.2°$) or to any other simple fluorite type superstructure, despite apparent fluorite-like zone axis DPs, e.g., Fig. 8d. Correct indexation of this phase is seriously complicated by the fact that, to a very good approximation, $a^* = \sqrt{3}/2b^*$ and $c^* = 2a^*\cos \beta^*$.

Integer indexation of the reciprocal lattice of the final phase in this system, type IV, requires four basis vectors given by $\mathbf{M}^* = \mathbf{a}^*$, $\mathbf{b}^*$, $\mathbf{c}^*$, and $\mathbf{q}$ respectively (Fig. 9). The I-centered monoclinic (pseudo-tetragonal) unit cell of the underlying average structure (most probable space group symmetry $I12/m1$) is given by $a \approx 3.90$, $b \approx 3.86$, $c \approx 5.20$ Å, $\beta \approx 91.3°$. The incommensurate primary modulation wavevector $\mathbf{q}$ is very close, but not exactly equal, to $\frac{1}{48}[2, 0, 36]^*$. The most probable superspace group symmetry is $I12/m1(0.04, 0, 0.75)\bar{1}1$. Typically, satellite reflections up to approximately eighth order are visible in $[0\,1\,0]$ zone axis DPs (Fig. 9a), rather less in XRD powder patterns. The previously published ($a_Z = 22.72$, $b_Z = 3.85$, $c_Z = 19.26$ Å, $\beta_Z = 101.9°$) monclinic cell (17) corresponds, in reciprocal space, to $\mathbf{a}_Z^* = \frac{1}{2}[0\,0\,\bar{6}\,8]^*$, $\mathbf{b}_Z^* = \frac{1}{2}[0\,2\,0\,0]^*$, and $\mathbf{c}_Z^* = \frac{1}{2}[0\,0\,\bar{2}\,2]^*$.

Bi_2O_3–WO_3. All phases in this system produced DPs with supercells of fluorite as reported (12). The space groups of types Ia and II could not be uniquely determined (choices of $I4$, $I\bar{4}$, $I4/m$, $I422$, $I4mm$, $I\bar{4}2m$, or $I4/mmm$ and $F4$, $F\bar{4}$, $F4/m$, $F422$, $F4mm$, $F\bar{4}2m$, or $F4/mmm$ respectively). Extinctions indicate $I4_1$ or $I4_122$ for type Ib. Note that an earlier XRD and single-crystal X-ray photographic study of type Ib (22) determined a higher symmetry, $I4_1/a$, for the same unit cell; this pseudo-symmetry condition rules out $I4_122$ (in a different Laue class to $I4_1/a$); therefore the space group must be $I4_1$.

Bi_2O_3–MoO_3. $Bi_{14}MoO_{24}$ was confirmed by ED to be isomorphous with the Bi_2O_3–WO_3 type Ia; a tetragonal superstructure of fluorite, $\mathbf{a} = \frac{3}{2}\mathbf{a}_f - \frac{1}{2}\mathbf{b}_f$, $\mathbf{b} = \frac{1}{2}\mathbf{a}_f + \frac{3}{2}\mathbf{b}_f$, $\mathbf{c} = 3\mathbf{c}_f$, space group $I{-}{-}{-}$ (Fig. 10). ED results reported for $Bi_{38}Mo_7O_{78}$ (11) were reproduced, and the supercell and space group confirmed ($Pccn$, uniquely determined from extinction conditions). $Bi_{26}Mo_{10}O_{69}$ was also investigated by ED, the $P2/c$ supercell reported (23) being observed. The relationship of this supercell to the fluorite-type δ-Bi_2O_3 subcell (not previously reported) was determined as $\mathbf{a} = \frac{3}{2}\mathbf{a}_f + \frac{3}{2}\mathbf{c}_f$, $\mathbf{b} = \mathbf{b}_f$, $\mathbf{c} = -4\mathbf{a}_f + 2\mathbf{c}_f$.
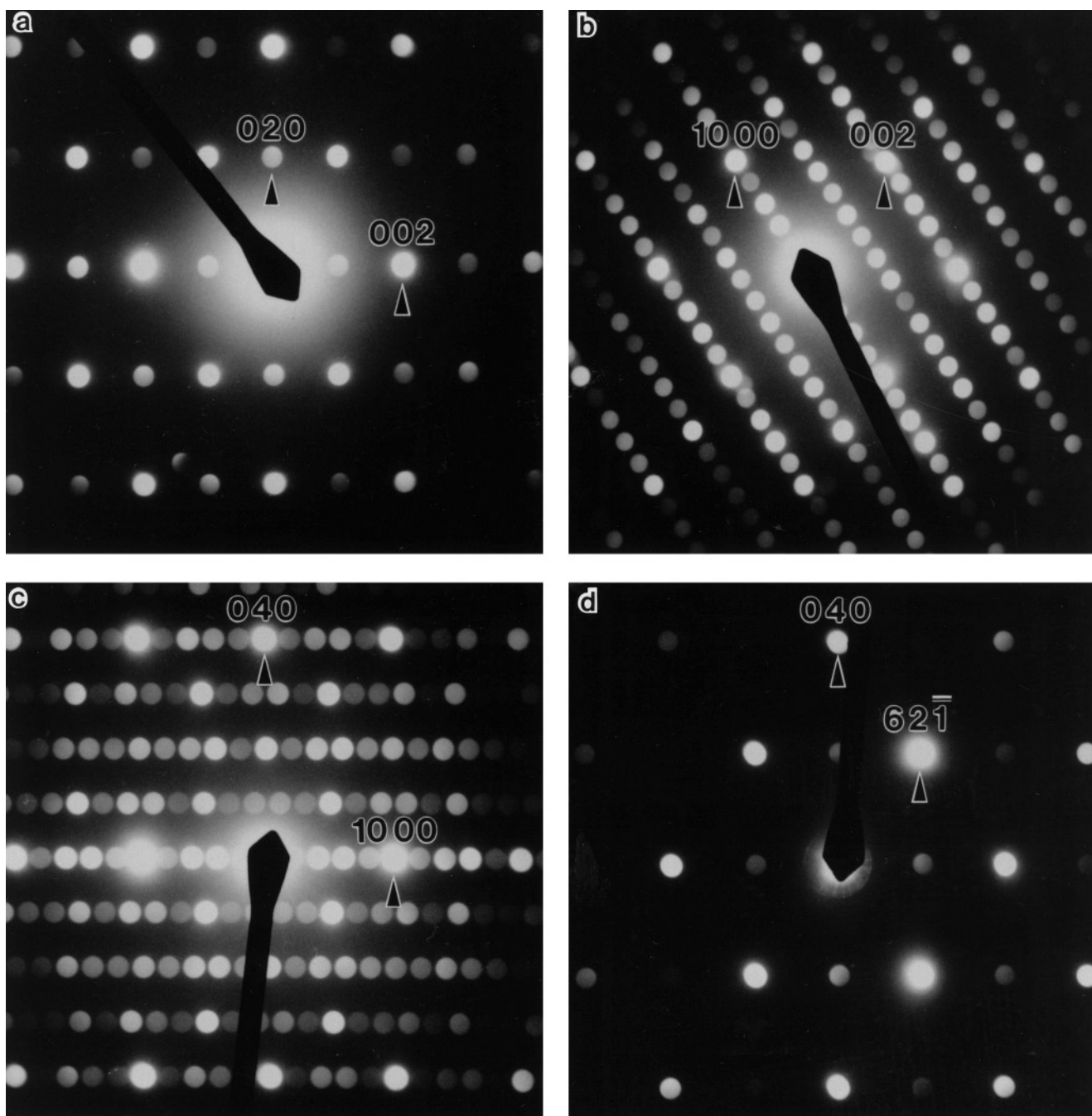
FIG. 7. (a) [1 0 0], (b) [0 1 0], (c) [0 0 1], and (d) [$\bar{1}$ 0 6] zone axis DPs of the type II* phase in the Bi$_2$O$_3$–Ta$_2$O$_5$ system.

Unit Cell/Subcell Refinement

Results of unit cell refinements are presented in Table 2. All refinements used synchrotron data with the exception of Bi$_{15}$TaO$_{25}$ and Bi$_{31}$Ta$_{17}$O$_{89}$, which used conventional XRD data.

Representative XRD patterns collected using synchrotron radiation ($\lambda = 1.4986$ Å) and presented below illustrate the various classes of structure (commensurately or incommensurately modulated, δ-Bi$_2$O$_3$-related or otherwise), exemplifying the quality of the data and the ability to index reflections with great confidence to high angle.
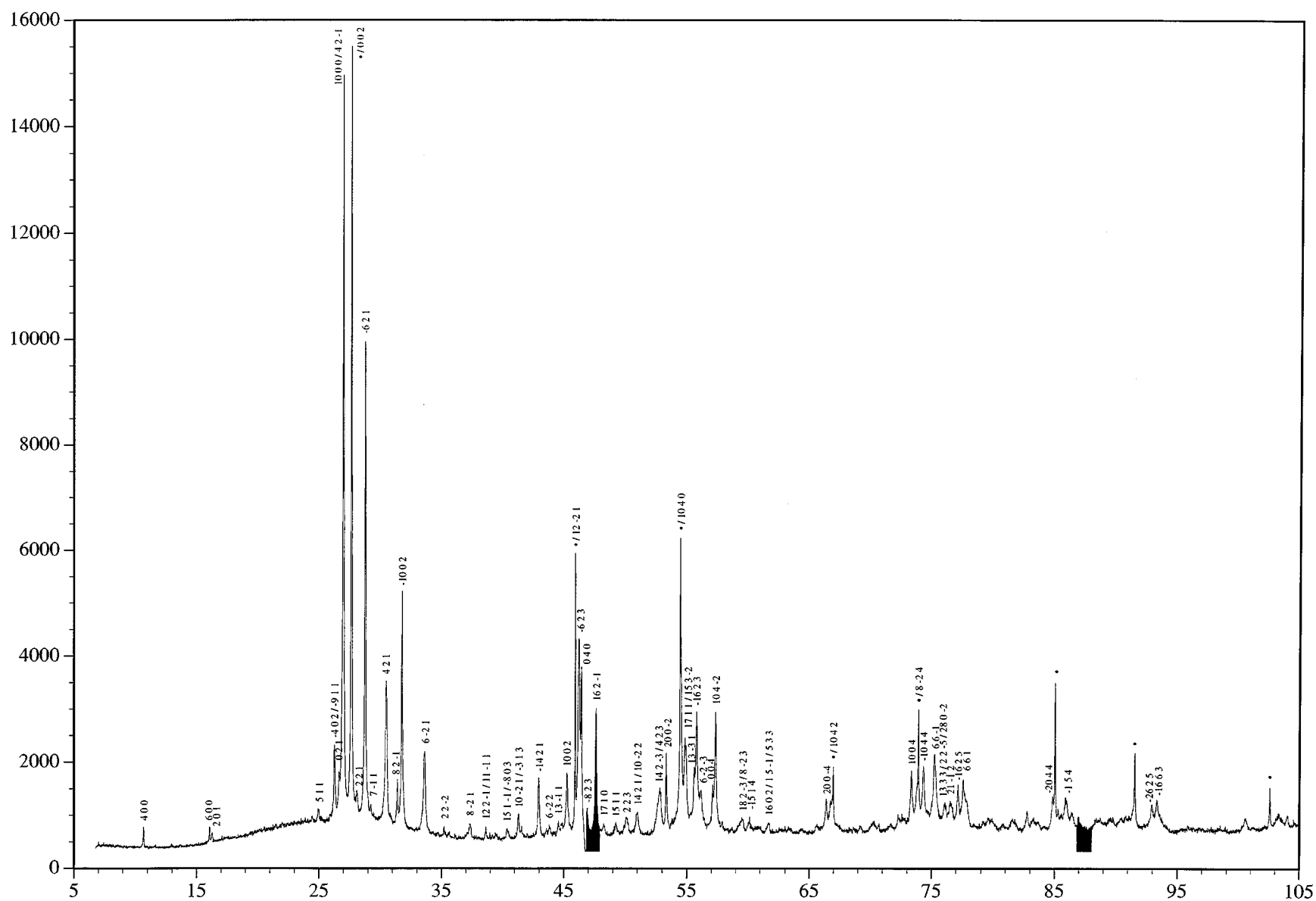
FIG. 13. XRD pattern collected using a synchrotron source ($\lambda = 1.4986$ Å) of $Bi_7Ta_3O_{18}$ indexed onto a monoclinic cell. Silicon standard reflections are marked (●).
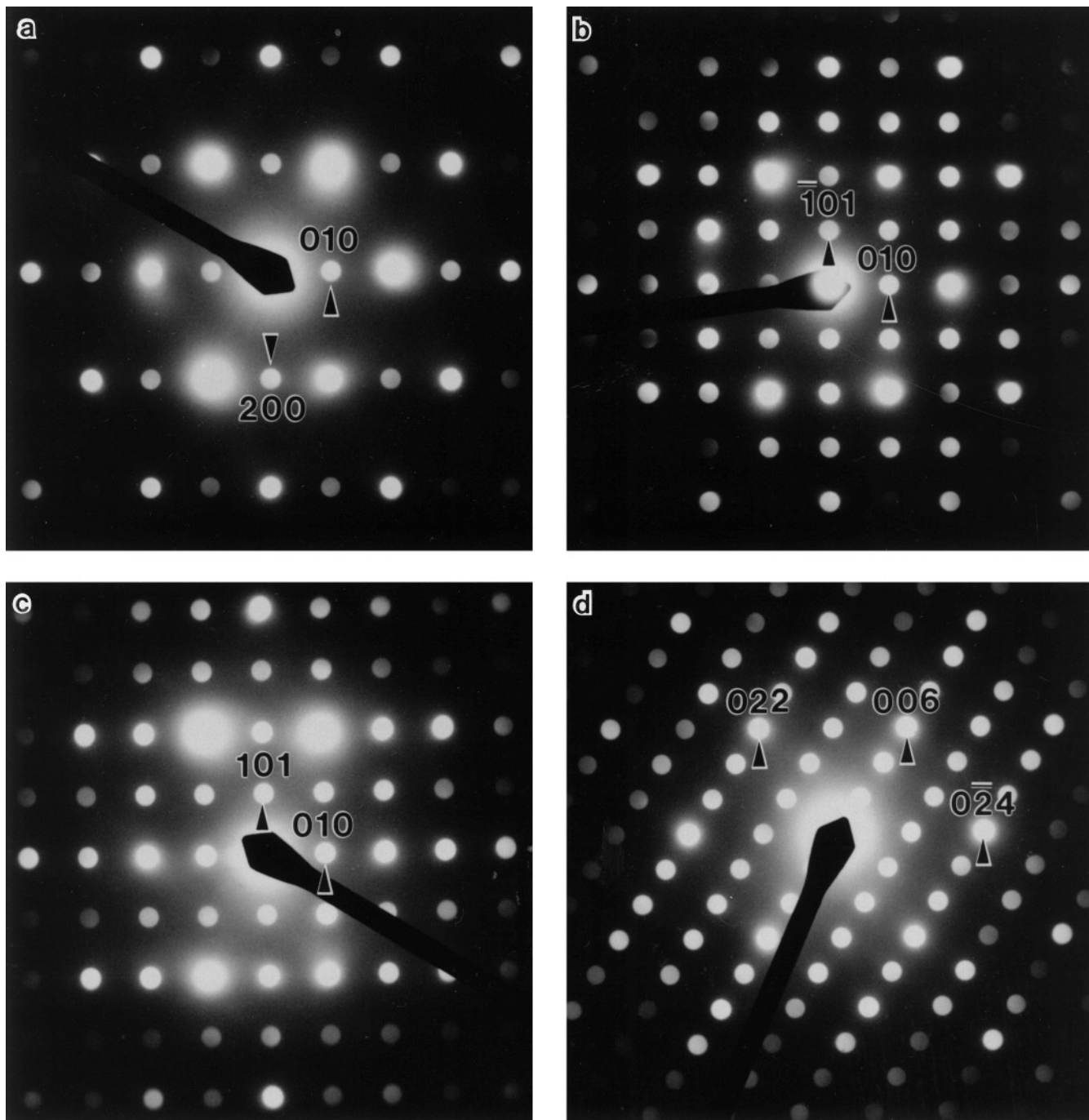
FIG. 8. (a) [0 0 1], (b) [1 0 1], (c) [$\bar{1}$ 0 1], and (d) [1 0 0] zone axis DPs of the type III phase in the Bi$_2$O$_3$–Ta$_2$O$_5$ system.

Figure 11 shows the XRD pattern for Bi$_8$Nb$_2$O$_{17}$, part of the type II solid solution, enlarged for the benefit of the observed modulation reflections. Reflections are indexed in six-dimensional notation. The eight modulation reflections observed and indexed are extremely weak; consider that the subcell reflection (1 1 1 0 0 0)* is off-scale by a factor of twenty. The weakness of the modulation reflections limited the ability of a previous study to model the structure using an incommensurate modulation wave approach (36).

The inset in Fig. 11 shows enlarged sections of XRD patterns from a range of type II solid solution phases, normalized to (1 1 1 0 0 0)* reflections, including the
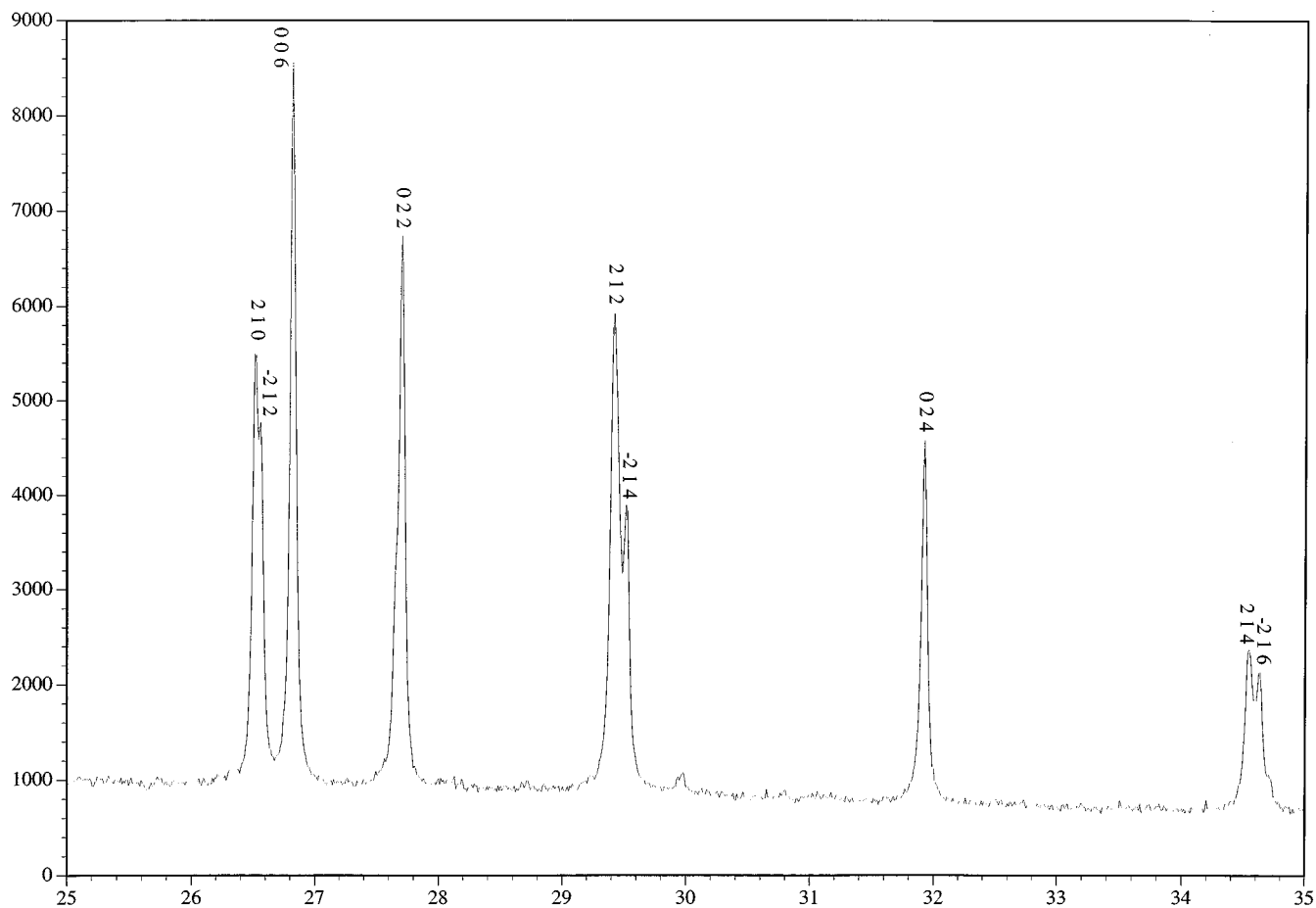
FIG. 14. XRD pattern collected using a synchrotron source ($\lambda = 1.4986$ Å) of $Bi_4Ta_2O_{11}$ indexed onto a metrically monoclinic cell (ED indicating the actual structure to be triclinic).

Nb_2O_5-rich end-member (determined by EDXA to be 23.4(4) mol% Nb_2O_5). The reflection arrowed is $(0\,0\,0\,1\,1\,1)^*$, which is the most intense of the first-order modulation reflections. The series indicates the rapid increase in modulation reflection intensity with increasing Nb_2O_5 content. The patterns also quantitatively confirm ED evidence for a monotonic increase in the incommensurate modulation parameter ε with Nb_2O_5 content; measured values of ε are given in the inset to Fig. 11.

A much greater number of modulation reflections are visible for $Bi_{14}W_2O_{27}$ (Fig. 12), and the fluorite subcell is distorted to face-centered tetragonal. Nonetheless, fluorite subcell reflections dominate and clearly justify classification as a modulated structure.

The pattern for monoclinic $Bi_7Ta_3O_{18}$ is shown in Fig. 13. Although strong reflections are grouped near fluorite subcell reflection positions, the relationship to fluorite is no longer obvious. Strong reflections in XRD are also strong in DPs (Fig. 1). As discussed above, there is no

unambiguous fluorite substructure accounting for all strong reflections, and we therefore question the previous assertion (19) that this phase is fluorite-related.

Figure 14 shows an enlarged section of the XRD pattern for $Bi_4Ta_2O_{11}$, highlighting (as for $Bi_7Ta_3O_{18}$) the ambiguities involved in correct indexation and finding a unique fluorite-related underlying substructure for these phases. The cell is in fact triclinic, as discussed in the electron diffraction section above, but very close to metrically monoclinic. In addition, $c^* = 2a^*\cos\beta^*$; this is the reason for the three narrowly split pairs of reflections in Fig. 14. The nine reflections indexed in Fig. 14 are of similar intensities, yet only seven unique reflections of any underlying fluorite substructure should be found in this region (four $\langle 1\,1\,1\rangle_f$ reflections and three $\langle 2\,0\,0\rangle_f$ reflections). The underlying substructure of this type III phase is therefore not (on average) fluorite-related.

Figure 15 shows the pattern for $Bi_{26}Mo_{10}O_{69}$. Again, there are groupings of strong reflections about the fluorite
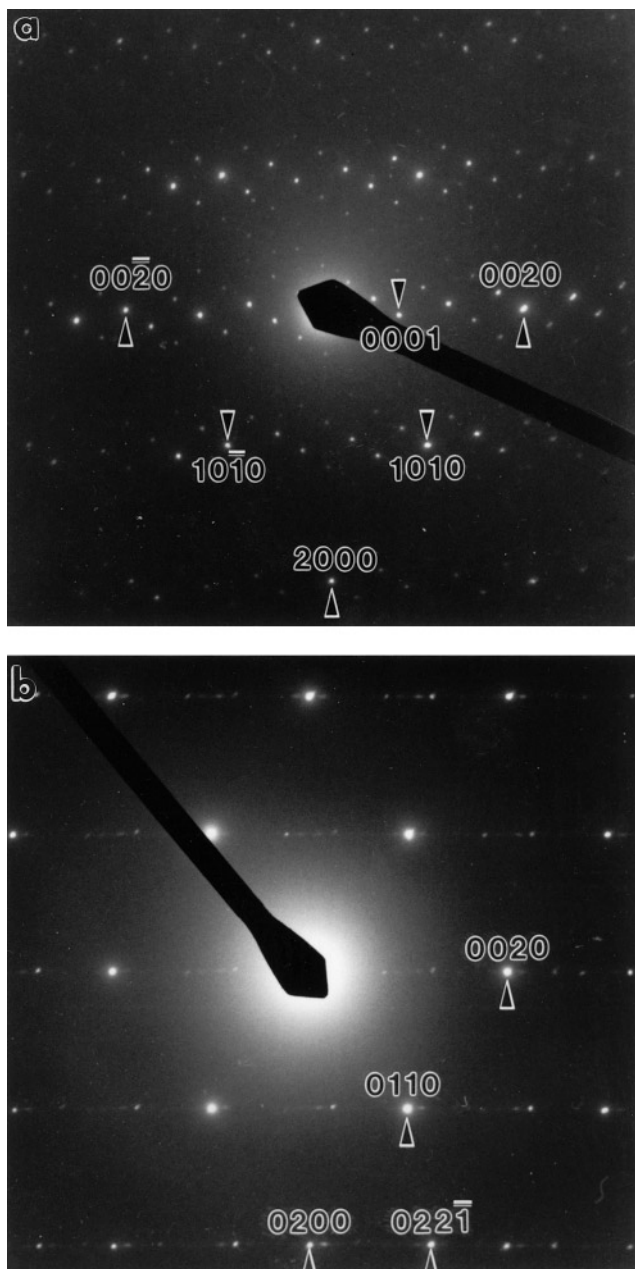
FIG. 9. (a) $[0\,1\,0]$ and (b) $[1\,0\,0]_f$ zone axis DPs of the type IV phase in the Bi$_2$O$_3$–Ta$_2$O$_5$ system.

FIG. 10. (a) $[3\,1\,0] \equiv [1\,0\,0]_f$ and (b) $[1\,\bar{1}\,0] \equiv [2\,\bar{4}\,0]_f$ zone axis DPs of the type Ia phase in the Bi$_2$O$_3$–MoO$_3$ system.

subcell reflection positions. Some modulation reflections are, however, of comparable intensity to subcell reflections, devaluing the expedience of a modulated structure description. This observation is borne out by the published structure of Bi$_{26}$Mo$_{10}$O$_{69}$ (23), the salient features of which are not (and need not be) discussed in terms of their relationship to fluorite-type δ-Bi$_2$O$_3$.

CONCLUSION

This reinvestigation of the systems Bi$_2$O$_3$–Nb$_2$O$_5$, Bi$_2$O$_3$–Ta$_2$O$_5$, Bi$_2$O$_3$–MoO$_3$, and Bi$_2$O$_3$–WO$_3$ is founded
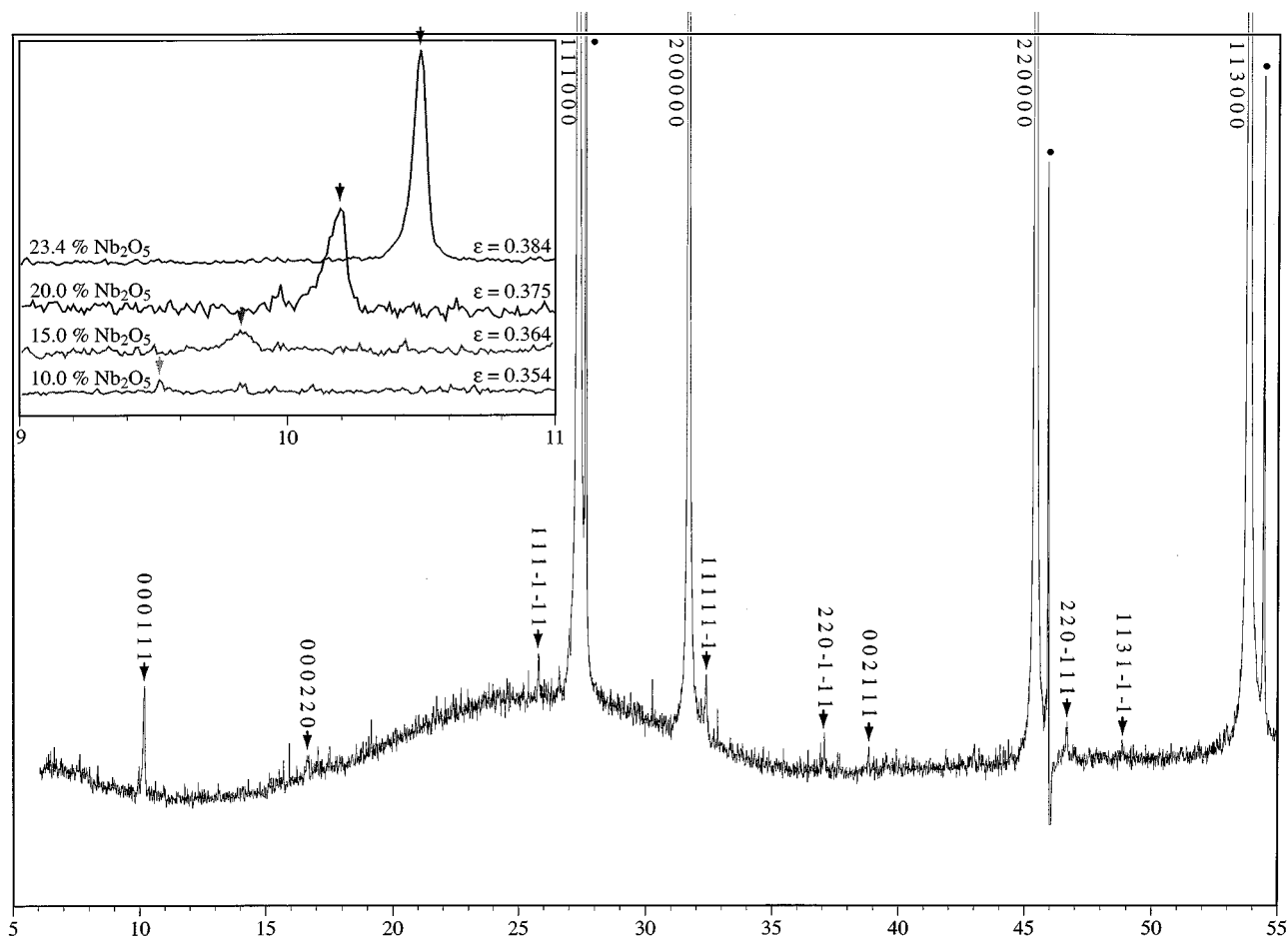
FIG. 11. XRD pattern collected using a synchrotron source ($\lambda = 1.4986$ Å) of $Bi_8Nb_2O_{17}$ indexed in six-dimensional notation (34). Silicon standard reflections are marked (●). The inset compares $(0\,0\,0\,1\,1\,1)^*$ reflections (normalized to $(1\,1\,1\,0\,0\,0)^*$ reflections) across the type II solid solution.

on careful, systematic methodology and the application of a range of complementary analytical techniques. It aims to resolve most of the confusion that has arisen when the results of previous studies are considered together. Given the internal consistency of our results, we believe that most of the problems identified in the Introduction have been resolved.

It is extremely difficult to index reflections correctly for large unit cell, low symmetry, commensurately modulated phases *ab initio* using XRD, and impossible for incommensurates. At the same time, indexing reciprocal lattices from ED alone may fail to identify multiphasic specimens or mistake impurity crystallites for those representative of the bulk specimen. Internal consistency between XRD and ED results is therefore essential.

Both XRD and ED results have helped indicate into which of two broad categories the phases investigated in this study fall; those with a fluorite-type δ-Bi_2O_3-related sub-structure, and those for which the average structure appears

to have moved too far from that prototype to be usefully described as a modulation thereof. Falling clearly in the former category are the type II solid-solutions in the Bi_2O_3–Nb_2O_5 and Bi_2O_3–Ta_2O_5 systems, $Bi_{15}TaO_{25}$ (type I), Bi_3NbO_7 (type III), $Bi_{14}WO_{24}$, and $Bi_{14}MoO_{24}$ (type Ia), $Bi_{46}W_8O_{93}$ (type II), and $Bi_{38}Mo_7O_{78}$. In the latter category are $Bi_5Nb_3O_{15}$ and $Bi_{31}Ta_{17}O_{89}$ (type IV), $Bi_7Ta_3O_{18}$ (type II*), $Bi_4Ta_2O_{11}$ (type III), and $Bi_{26}Mo_{10}O_{69}$.

Where possible, a modulated structure approach should be used in structural studies of these phases. The important advantage of a modulated structure approach is the ability to recognize and confidently index complex XRD patterns by virtue of the hierarchy of intensities associated with this modulated structure description. In single-crystal structural studies, this translates to a reduction in the number of variables by eliminating the need to consider structural degrees of freedom associated with higher order modulation reflections having zero observed intensity.
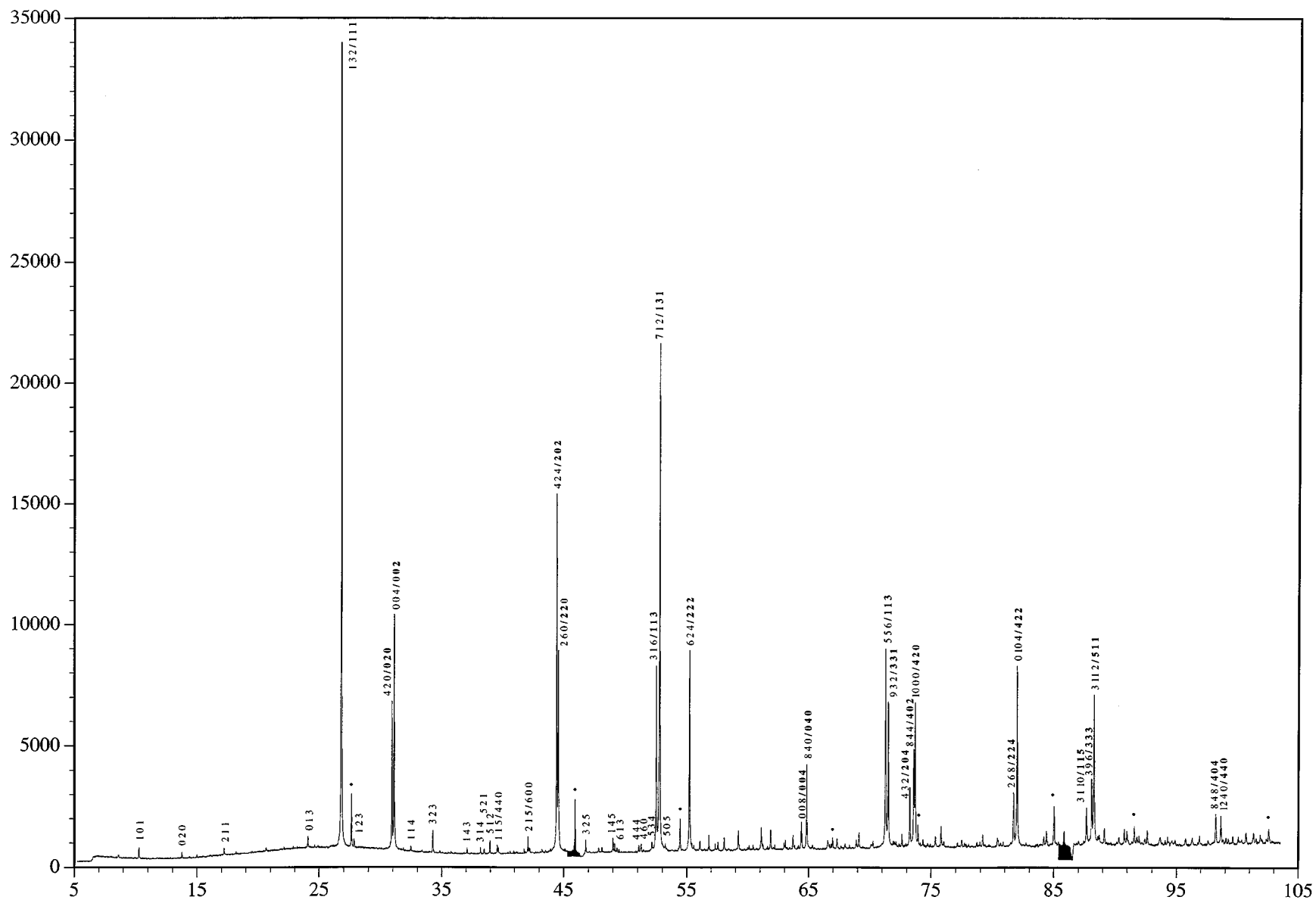
FIG. 12. XRD pattern collected using a synchrotron source ($\lambda = 1.4986$ Å) of $Bi_{14}W_2O_{27}$ indexed onto a tetragonal cell. Silicon standard reflections are marked (●) and reflections of the fluorite subcell are indexed in bold type.
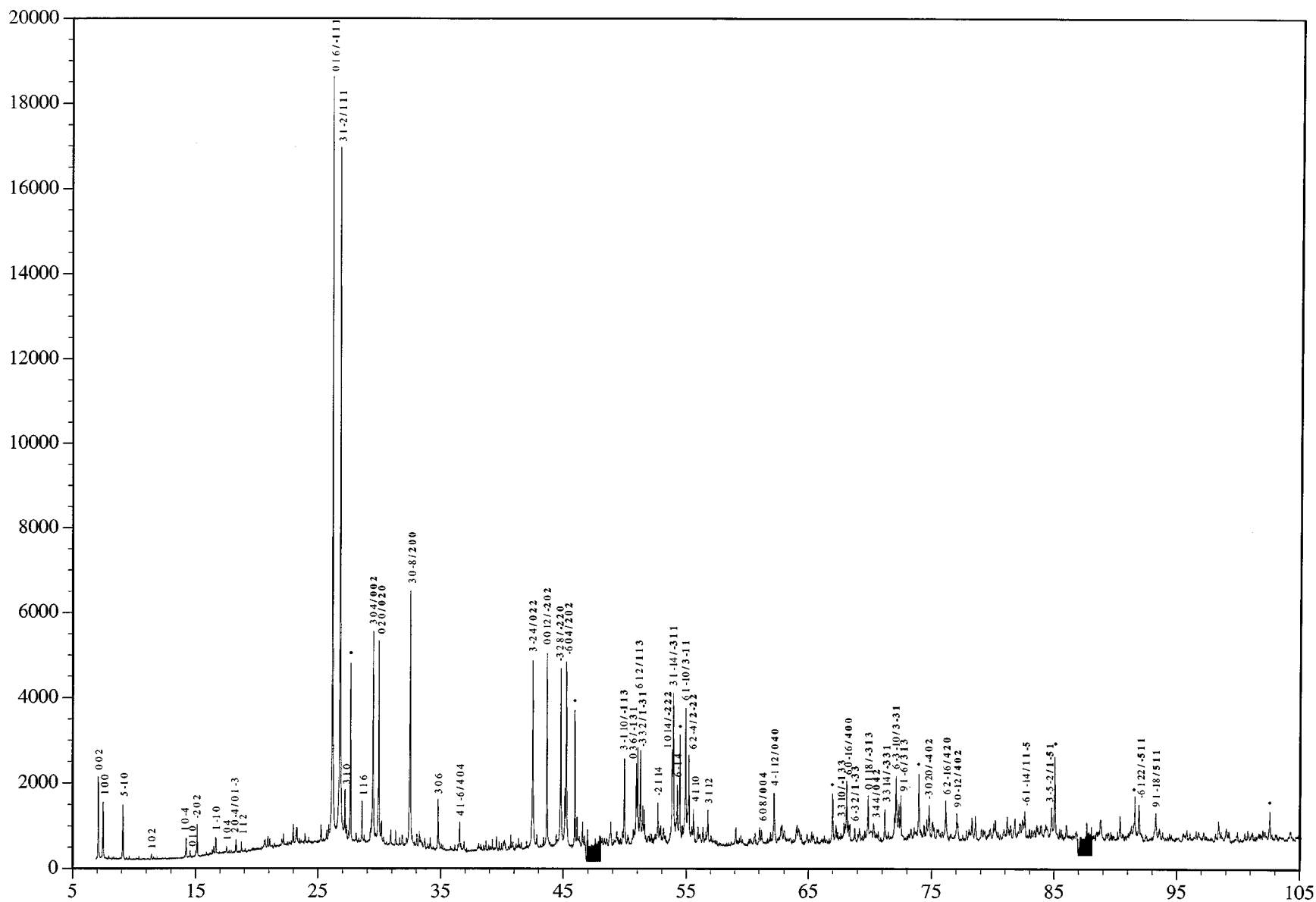
FIG. 15. XRD pattern collected using a synchrotron source ($\lambda = 1.4986$ Å) of $Bi_{26}Mo_{10}O_{69}$ indexed onto a monoclinic cell. Silicon standard reflections are marked (●) and reflections of the fluorite subcell are indexed in bold type.

REFERENCES

1. T. Takahashi and H. Iwahara, *Mater. Res. Bull.* **13,** 1447 (1978).
2. A. W. Sleight, *Science* (1980).
3. A. R. Allnat and P. W. M. Jacobs, *Proc. R. Soc. London Ser.* A**260,** 350 (1961).
4. A. R. Allnat and P. W. M. Jacobs, *Chem. Rev.* **67,** 681 (1967).
5. G. Gattow and H. Schröder, *Z. Anorg. Allg. Chem.* **318,** 176 (1962).
6. H. A. Harwig, *Z. Anorg. Allg. Chem.* **444,** 151 (1978).
7. G. Gattow and H. Fricke, *Z. Anorg. Allg. Chem.* **324,** 287 (1962).
8. R. S. Roth and J. L. Waring, *Am. Miner.* **48,** 1348 (1963).
9. A. C. Skapski and D. Rogers, *J. Chem. Soc. Chem. Commun.* 611 (1965).
10. J. G. Thompson, S. Schmid, R. L. Withers, A. D. Rae, and J. D. Fitzgerald, *J. Solid State Chem.* **101,** 309 (1992).
11. D. J. Buttrey, D. A. Jefferson, and J. M. Thomas, *Mater Res. Bull.* **21,** 739 (1986).
12. W. Zhou, *J. Solid State Chem.* **108,** 381 (1994).
13. W. Zhou, D. A. Jefferson, and J. M. Thomas, *Proc. Roy. Soc. London* **A406,** 173 (1986).
14. W. Zhou, D. A. Jefferson, and J. M. Thomas, *J. Solid State Chem.* **70,** 129 (1987).
15. D. Tang and W. Zhou, *J. Solid State Chem.* **119,** 311 (1995).
16. W. Zhou, D. A. Jefferson, M. Alario-Franco, and J. M. Thomas, *J. Phys. Chem.* **91,** 512 (1987).
17. W. Zhou, D. A. Jefferson, and J. M. Thomas, *Geophys. Monogr.* **43,** 113 (1989).
18. J. Gopalakrishnan, A. Ramanan, C. N. R. Rao, D. A. Jefferson, and D. J. Smith, *J. Solid State Chem.* **55,** 101 (1984).
19. W. Zhou, *J. Solid State Chem.* **101,** 1 (1992).
20. O. Savborg and M. Lundberg, *J. Solid State Chem.* **57,** 135 (1985).
21. E. Aguardo, R. Enjalbert, J. M. Rojo, and A. Castro, *Bol. Soc. Esp. Cerám. Vidrio* **34** [5–6], 417 (1995).
22. A. Watanabe, N. Ishizawa, and M. Kato, *J. Solid State Chem.* **60,** 252 (1985).
23. R. N. Vannier, G. Mairesse, F. Abraham, and G. Nowogrocki, *J. Solid State Chem.* **122,** 394 (1996).
24. R. S. Roth and J. Waring, *J. Research Natl. Bur. Standards* **66A** (6), 461 (1962).
25. E. M. Levin and R. S. Roth, *J. Research Natl. Bur. Standards* **68A** (2), 202 (1964).
26. A. C. Larson and R. B. Von Dreele, "*GSAS: The General Structure Analysis System*" Los Alamos National Laboratory, 1991.
27. E. M. Levin and R. S. Roth, *J. Research Natl. Bur. Standards* **68A** [2], 197 (1964).
28. E. T. Keve and A. C. Skapski, *J. Solid State Chem.* **8,** 159 (1973).
29. E. I. Speranskaya, *Inorg. Mater.* (*Engl. Transl.*) **6** (1), 127 (1970).
30. M. Egashira, K. Matsuo, S. Kagawa, and T. Seiyama, *J. Catal.* **58** (3), 409 (1979).
31. J. M. Perez-Mato, G. Madariaga, F. J. Zuñiga, and A. Garcia Arribas, *Acta Cryst* A**43,** 216 (1987).
32. S. Van Smaalen, *Cryst. Rev.* **4,** 79 (1995).
33. T. Jannsen, A. Janner, A. Looijenga-Vos, and P. M. DeWolff, "Incommensurate and commensurate modulated structures," International Tables for Crystallography Vol. C. A. J. C. Wilson, Ed. Kluwer Academic Publishers, Dordrecht, 797, 1992.
34. A. Yamamoto, *Acta Crystallogr. Sect. B* **38,** 1451 (1982).
35. R. L. Withers, Y. C. Feng, and G. H. Lu, *J. Phys.: Condens. Matter* **2,** 3187 (1990).
36. R. Miida and M. Tanaka, *Jpn. J. Appl. Phys.* **29** (6), 1132 (1990).
37. R. L. Withers, J. G. Thompson, P. J. Barlow, and J. C. Barry, *Aust. J. Chem.* **45,** 1375 (1992).
38. A. Pring, T. Williams, and R. L. Withers, *Amer. Miner.* **78,** 619 (1993).